https://doi.org/10.5194/essd-2026-563
Preprint. Discussion started: 23 September 2026

A National Depth-Resolved Soil-Moisture-to-Electromagnetic Proxy Database for Hydrogeophysical Monitoring

Diaa Sheishah[1, 2]*, Enas Abdelsamei[1, 2], Viktória Blanka-Végi[1], Károly Barta[1], Ahmed M. Ali[1,2], Khaldoun Abualhin[4], Djamil Al-Halbouni[4], Wouter Dorigo[3], György Sipos[1]*

[1]University of Szeged, Department of Physical and Environmental Geography, 6722 Szeged, Egyetem u. 2-6., Hungary

geo diaa@nriag.sci.eg, enas.mohammed@nriag.sci.eg, blankav@geo.u-szeged.hu, barta@geo.u-szeged.hu, ahmed.mahmoud@nriag.sci.eg , gysipos@geo.u-szeged.hu

[2]National Research Institute of Astronomy and Geophysics, 11421, El Marsad st., Helwan, Cairo, Egypt

[3]Department of Geodesy and Geoinformation, Technische Universitaet Wien (TU Wien), Vienna, Austria

wouter.dorigo@tuwien.ac.at

[4]Institute for Earth System Science and Remote Sensing, University of Leipzig, Talstr. 35, 04103 Leipzig, Germany

dhalbouni@uni-leipzig.de , khaldoun_salman.abualhin@uni-leipzig.de

Corresponding authors: Diaa Sheishah geo diaa@nriag.sci.eg & György Sipos gysipos@geo.u-szeged.hu

Abstract

Soil moisture is a key control on drought, recharge, crop water availability, agricultural water management, and land-atmosphere exchange, but its depth-resolved spatial variability remains difficult to monitor over large areas. Non-invasive methods such as ground-penetrating radar (GPR), electrical resistivity, and electromagnetic surveys can support soil-moisture estimation, yet their interpretation depends strongly on soil texture and hydraulic-retention properties. This study develops a national six-depth soil-moisture-to-electromagnetic proxy database to support future GPR- and resistivity-based root-zone monitoring and decision support. We used multi-year soil-moisture, porosity, saturation, texture, and hydraulic-retention data from 117 monitoring stations across Hungary at 10, 20, 30, 45, 60, and 75 cm depth. Dielectric permittivity, EM-wave velocity, electrical conductivity, attenuation, and apparent resistivity were derived as proxy variables from observed soil moisture using established petrophysical relationships, including the Topp equation and an Archie-type formulation. The proxy database identified a consistent 30-45 cm buffering zone, where soil moisture increased to 22.25%, dielectric permittivity peaked at 12.29, EM-wave velocity reached a minimum of 0.0935 m ns^{-1}, and apparent resistivity decreased to 545 Ω m. Texture strongly shaped the translated EM response: sandy soils were lower-moisture and more resistive, whereas clayey soils retained more water and showed higher dielectric response. Hydraulic-retention variables provided calibration-relevant prior information for explaining why similar EM or resistivity signals may

https://doi.org/10.5194/essd-2026-563
Preprint. Discussion started: 23 September 2026

Earth System Science Data Discussions
Open Access

represent different true soil-moisture values across soil types. The framework provides a transferable national calibration layer for drought-monitoring agencies, irrigation planners, precision-agriculture users, and future drone-based geophysical surveys in regions with comparable monitoring and soil databases.

Keywords: Soil moisture; Hydrogeophysical parameters; Hydraulic retention; Machine learning, explainable 3D Hydrogeophysical state model

1. Introduction

Soil moisture (SM) is a central state variable of the vadose zone because it regulates water storage, infiltration, evapotranspiration, groundwater recharge, crop water availability, and soil–plant–atmosphere exchange (Hsu & Dirmeyer 2023; He et al. 2023; Zhou et al. 2024). Yet its vertical and spatial organization remains difficult to characterize, particularly across heterogeneous soil profiles where texture, porosity, hydraulic retention, structure, climate forcing, land use, and antecedent soil-moisture conditions interact. Hydrogeophysical (HG) approaches provide a powerful framework for investigating these processes because soil water strongly affects dielectric permittivity (ε_r), EM-wave velocity (v), electrical conductivity (σ), attenuation (α), and apparent resistivity (ρ_a). Ground-penetrating radar (GPR), electrical resistivity tomography (ERT), Electromagnetic (EM) induction, and related methods have therefore become increasingly important for non-invasive assessment of soil-water dynamics and vadose-zone structure (Vereecken et al., 2008; Zhou et al., 2001; Tartakovsky et al., 2008; Steelman et al., 2012; Cheng et al., 2023; Jadoon et al., 2012; Abbas et al., 2022; Zou et al., 2023; Sheishah et al., 2023a; Sheishah et al., 2023b; Yu et al., 2026; Sheishah et al., 2026a).

Recent HG research has moved from qualitative geophysical interpretation toward physically constrained estimation of water content and soil hydraulic properties. Time-lapse GPR and coupled inversion studies have shown that soil hydraulic parameters can be inferred from geophysical responses when hydrological and EM models are linked (Jadoon et al., 2008; Mboh et al., 2012; Jadoon et al., 2012; Busch et al., 2013; Yu et al., 2022; Yu et al., 2026). Similarly, integrated GPR–ERT experiments have demonstrated that wetting fronts can be monitored through paired increases in ε_r and decreases in electrical resistivity (Zhou et al., 2001; Hayley et al., 2009; Zou et al., 2023; Sheishah et al., 2026b; Abdelsamei et al., 2024), while petrophysical frameworks such as Archie's law and the Complex Refractive Index Model (CRIM) provide mechanistic links between saturation, porosity, resistivity, and permittivity (Abbas et al., 2022). Field-scale GPR studies have also confirmed strong dielectric–soil-water

https://doi.org/10.5194/essd-2026-563
Preprint. Discussion started: 23 September 2026

relationships, particularly in the upper root zone (Cao et al., 2020). However, these relationships are not universal: resistivity-derived soil-water estimates depend on texture, land use, depth, high- and low-moisture states, pore-water resistivity, porosity, saturation, and temperature (Sun et al., 2020).

A parallel development has emerged in soil hydrology and soil health assessment. Static indicators such as saturated hydraulic conductivity, available water content, clay content, organic matter, bulk density, and soil depth are increasingly used to infer water-regulation services, but their relationships with infiltration, recharge, runoff generation, and crop water stress are often nonlinear and context-dependent (Yosef et al., 2026). Earlier and recent irrigation and soil-water studies similarly show that hydraulic characterization is essential for interpreting water availability and irrigation response (Patil & Rajput, 2009; Finkenbiner et al., 2019; Hassan et al., 2024). In Hungary, functional evaluation of soil hydraulic parameterizations has further shown that local soil hydraulic information and detailed vertical discretization can improve soil-moisture and water-budget simulations (Hoylman et al., 2019; Peterson et al., 2019; Kozma et al., 2024). These findings imply that future EM- or resistivity-based soil-moisture estimation should not rely on a single moisture-to-signal relationship, but should be conditioned by hydraulic-retention architecture and soil texture.

Machine learning has opened additional possibilities for modelling these relationships, particularly where soil–water–EM interactions are nonlinear. Random Forests and related ensemble methods provide robust tools for handling complex predictor structures (Breiman, 2001). In HG, artificial neural networks have been shown to capture the nonlinear relationship between σ and SM more effectively than fixed petrophysical models (Moghadas & Badorreck, 2019). In soil and geotechnical applications, machine learning and explainable AI have also demonstrated that depth-dependent soil profile properties, including field capacity, hydraulic conductivity, and related retention variables, can provide strong predictive information (Achu et al., 2026). Recent soil-hydrological studies have also shown that saturated hydraulic conductivity is a key hydraulic descriptor for interpreting soil-water regulation and landscape-scale water movement (Pan et al., 2023). These studies highlight the potential of ML for HG interpretation, but they also underline the need to avoid circular modelling, where variables derived from soil moisture are used to predict other variables derived from the same soil-moisture signal.

Despite these advances, three major research gaps remain. First, future drone GPR, resistivity, and EM-induction surveys lack a national, depth-resolved reference database linking routinely monitored soil moisture to expected EM-property ranges under contrasting soil textures (He et al., 2023; Bo et al., 2026). Second, the role of texture and hydraulic retention in controlling water storage is still not sufficiently translated into practical calibration information for estimating true SM from non-invasive EM or resistivity measurements. Texture provides a first-order control, while water-holding capacity, field capacity, wilting point, and hygroscopic retention describe the pore-scale storage conditions that cause similar EM responses to represent different SM values across soils. Third, integrated proxy indices capable of summarizing vertical buffering, propagation resistance, dielectric contrast, velocity damping, and spatial calibration provinces remain underdeveloped, especially when evaluated with leakage-safe models that avoid using SM-derived variables to predict other SM-derived variables.

Accordingly, this study addresses the following research questions: (i) How can a national, six-depth SM monitoring network be translated into a consistent EM proxy database for future GPR, resistivity, and EM surveys? (ii) How do texture and hydraulic-retention properties affect water storage and the resulting SM-derived EM proxy ranges across the 10-75 cm root-zone profile? (iii) Can integrated proxy indices identify vertical buffering zones and spatial calibration provinces across the national monitoring network? (iv) Which retention and texture variables provide useful prior information for estimating true SM from future independent EM or resistivity measurements without circular dependence on SM-derived predictors?

The aim of this study is to develop a national-scale, multi-year, six-depth SM-to-EM proxy database that can support future non-invasive soil-moisture estimation by drone GPR, resistivity, and related EM methods. Specifically, we: (i) translate observed SM, porosity, saturation, and texture information into EM proxy variables using established petrophysical relationships; (ii) quantify the vertical, seasonal, and texture-dependent structure of SM and the derived proxy variables ε_r, v, σ, α, and ρ_a; (iii) evaluate how textural properties and retention metrics affect water storage and therefore the expected EM response; (iv) develop integrated indices for vertical buffering, propagation resistance, dielectric attenuation, velocity damping, and resistivity gradients; (v) map national-scale proxy provinces using station-level spatial interpolation; and (vi) test leakage-safe machine-learning models using only retention, grain-size, and texture predictors as prior information for future EM-to-SM calibration. Together, these gaps motivate a national, depth-resolved SM-to-EM proxy database that links measured soil moisture, soil texture, hydraulic-retention properties, and derived electromagnetic proxy variables under a leakage-safe modelling framework.

https://doi.org/10.5194/essd-2026-563
Preprint. Discussion started: 23 September 2026

2. Data Source and Monitoring Network

This study used data from the Hungarian Operational Drought and Water Scarcity Monitoring System (DWMS), established in 2016 by the Hungarian General Directorate of Water Management and publicly available through DWMS platforms (Fiala et al., 2018; Fiala et al., 2018b; Operational Drought Monitoring System, n.d.; OVF, 2024; ODMS). The DWMS provides high-resolution in situ soil-moisture observations across six depths (10, 20, 30, 45, 60, and 75 cm), together with soil-temperature profiles, meteorological information, drought-monitoring indicators, and site-specific soil properties, including hydraulic-retention and grain-size characteristics. The present analysis used 117 automated DWMS stations distributed across Hungary (Fig. 1), providing national-scale coverage of contrasting soil textures, land-use settings, and hydroclimatic conditions. This monitoring network therefore provides measured soil-moisture and soil-property information, not direct geophysical measurements. In this study, the measured SM, porosity, saturation, texture, and retention variables were used to derive electromagnetic proxy variables, including ε_r, v, σ, α, and ρ_a. The resulting database was designed as a national reference layer for future drone GPR, resistivity, and EM-based soil-moisture estimation. Raw DWMS observations are publicly available through the operational DWMS platforms, and the processed variables and derived proxy indices used in this study are described in the Open Research statement.

https://doi.org/10.5194/essd-2026-563
Preprint. Discussion started: 23 September 2026

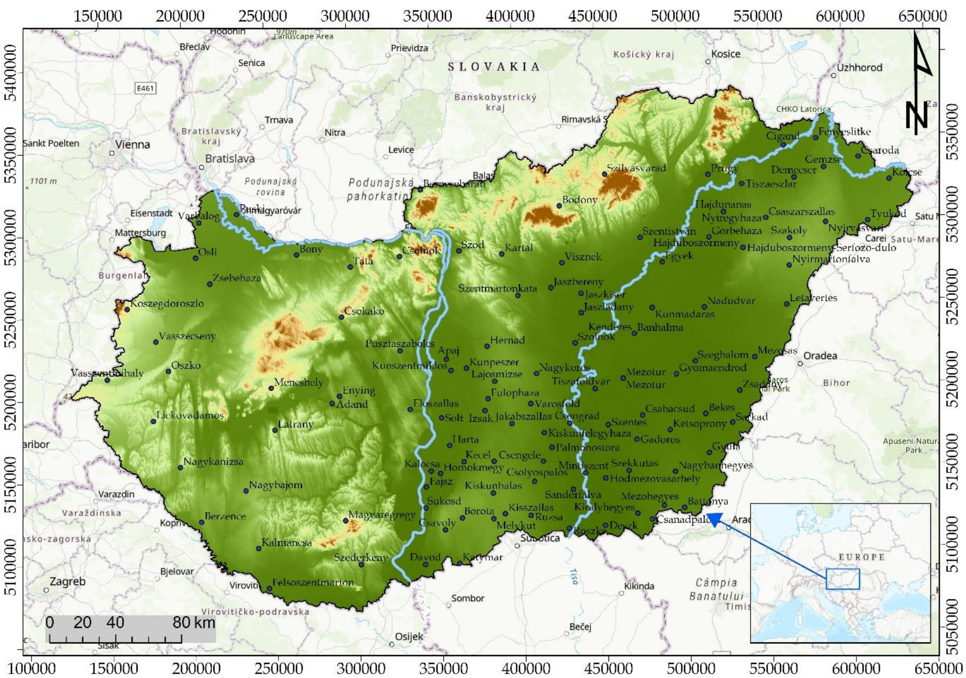

Figure 1. Spatial distribution of the drought monitoring stations used in this study across Hungary. The map was prepared in ArcGIS Pro using DWMS station locations from the national Operational Drought and Water Scarcity Monitoring Network, operated by the Hungarian General Directorate of Water Management (OVF). The map includes the national boundary, major river network, elevation/hillshade context, and an inset location map to show the regional setting. Stations provide representative coverage of Hungary's diverse hydro-climatic and soil conditions and form the basis for station-wise time-series analysis and model development. Basemap and hillshade layers are from ArcGIS Online/Esri World Topographic Map and World Hillshade, with attribution to Esri, OpenStreetMap contributors, and associated data providers.

3. Materials and methods

The complete analytical workflow is summarized in Fig. 2. The methodology was designed to transform measured multi-depth SM observations and soil-property data into physics-informed EM proxy variables, evaluate their vertical, seasonal, textural, and spatial organization, and test whether texture and hydraulic-retention properties provide independent prior information for future EM-to-SM calibration. Because ε_r, v, σ, α, and ρ_a were derived from SM through petrophysical equations, they are interpreted as proxy variables rather than independent

https://doi.org/10.5194/essd-2026-563
Preprint. Discussion started: 23 September 2026

geophysical observations. The processed input data, derived hydrogeophysical proxy variables, and reproducible analysis scripts associated with this workflow are archived in Zenodo (Sheishah et al., 2026c).

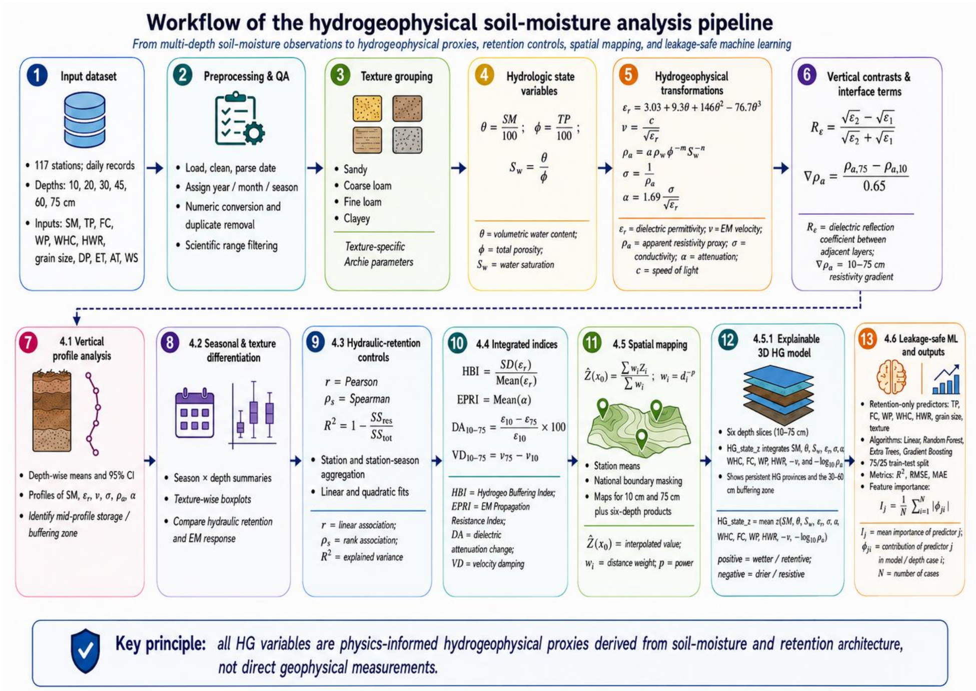

Fig. 2. Workflow of the SM-to-EM proxy database pipeline. The workflow shows the main steps from multi-depth soil-moisture data processing to EM proxy derivation, vertical and texture-based analysis, retention assessment, spatial mapping, and leakage-safe machine-learning evaluation for future GPR, resistivity, and EM survey calibration.

3.1 EM proxy derivation and vertical profile analysis

The analysis used daily station-wise SM and soil hydraulic data from 117 monitoring stations at six depths: 10, 20, 30, 45, 60 and 75 cm. The input variables included SM, total porosity (TP), field capacity (FC), wilting point (WP), water-holding capacity (WHC), hygroscopic water-retention variables (HWR), grain-size fractions, precipitation (DP), evapotranspiration (ET), air temperature (AT), and water-scarcity indicators (WS). Dates were parsed into year, month and season, numerical variables were converted to numeric format, duplicates were removed, and physically unrealistic derived values were filtered before statistical analysis. Sand, silt, and clay percentages were first processed using an Excel-based workflow and plotted within the USDA soil texture triangle (Natural Resources Conservation Service, n.d.) to

https://doi.org/10.5194/essd-2026-563
Preprint. Discussion started: 23 September 2026

determine the textural class of each station. Stations were then grouped into sandy, coarse loam, fine loam, and clayey soil categories. Texture-specific Archie parameters were assigned to these groups as scenario assumptions rather than calibrated site-specific constants. This grouping supported interpretation of texture-dependent water storage and of the expected EM proxy response under future independent geophysical measurements.

For each station s, date t, and depth z, soil moisture was converted to volumetric water content, porosity was derived from total porosity, and water saturation (S_w) was calculated as:

$$\theta_{s,t,z} = \frac{SM_{s,t,z}}{100}, \phi_{s,z} = \frac{TP_{s,z}}{100}, S_{w,s,t,z} = \frac{\theta_{s,t,z}}{\phi_{s,z}} \qquad (1)$$

where $\theta_{s,t,z}$ is volumetric water content, $SM_{s,t,z}$ is measured soil moisture (%), $\phi_{s,z}$ is total porosity, $TP_{s,z}$ is total porosity (%), and $S_{w,s,t,z}$ is water saturation.

Relative ε_r was translated from volumetric water content using the empirical Topp equation (Topp et al., 1980):

$$\varepsilon_{r,s,t,z} = 3.03 + 9.30\theta_{s,t,z} + 146.0\theta_{s,t,z}^2 - 76.7\theta_{s,t,z}^3 \qquad (2)$$

where $\varepsilon_{r,s,t,z}$ is relative ε_r and $\theta_{s,t,z}$ is volumetric water content.

v was calculated from $\varepsilon_{r,s,t,z}$ following the standard GPR velocity relationship for non-magnetic materials (Huisman et al., 2003):

$$v_{s,t,z} = \frac{c}{\sqrt{\varepsilon_{r,s,t,z}}} \qquad (3)$$

where $v_{s,t,z}$ is EM wave velocity and $c = 0.299$ m ns^{-1} is the speed of light in vacuum.

Apparent bulk resistivity was estimated as a scenario-based proxy using an Archie-type formulation (Archie, 1942):

$$\rho_{a,s,t,z} = a_z \rho_w \phi_{s,z}^{-m_z} S_{w,s,t,z}^{-n_z} \qquad (4)$$

where $\rho_{a,s,t,z}$ is the apparent resistivity proxy, a_z, m_z, and n_z are texture-dependent Archie parameters, ρ_w is the assumed pore-water resistivity, $\phi_{s,z}$ is total porosity, and $S_{w,s,t,z}$ is water saturation. For clayey and fine-loam soils, these Archie-based ρ_a estimates should be interpreted cautiously because clay-mineral surface conduction can affect resistivity independently of pore-water saturation.

ε_r and α were then derived as:

$$\sigma_{s,t,z} = \frac{1}{\rho_{a,s,t,z}}, \alpha_{s,t,z} = 1.69\frac{\sigma_{s,t,z}}{\sqrt{\varepsilon_{r,s,t,z}}} \qquad (5)$$

https://doi.org/10.5194/essd-2026-563
Preprint. Discussion started: 23 September 2026

where $\sigma_{s,t,z}$ is the conductivity proxy, $\rho_{a,s,t,z}$ is the ρ_a proxy, $\alpha_{s,t,z}$ is the α proxy, and $\varepsilon_{r,s,t,z}$ is relative ε_r.

These derived variables represent a physics-informed SM-to-EM proxy translation and should not be interpreted as direct field measurements of ε_r, v, σ, α, or ρ_a.

Depth-wise vertical profiles of SM, ε_r, v, σ, ρ_a, and α were summarized using the mean and 95% confidence interval:

$$\bar{x}_z = \frac{1}{n_z}\sum_{i=1}^{n_z} x_{i,z}\,, CI_{95,z} = 1.96\frac{s_z}{\sqrt{n_z}} \tag{6}$$

where $\bar{x}_z$ is the mean value at depth z, $x_{i,z}$ is observation i at depth z, n_z is the number of valid observations, s_z is the standard deviation, and $CI_{95,z}$ is the 95% confidence interval.

3.2 Seasonal and texture-dependent proxy differentiation

Seasonal and texture-dependent proxy differentiation was evaluated to describe how measured SM and soil texture translate into expected EM-property ranges. For each season–depth and texture–depth combination, the variables derived in Eqs. (1)–(5) were summarized using Eq. (6). Seasonal–depth heatmaps were produced for SM, ε_r, v, ρ_a, σ, and α, while texture-wise boxplots were generated to compare sandy, coarse-loam, fine-loam and clayey soils across all six depths. This allowed the observed moisture regime and the corresponding SM-derived EM proxy response to be evaluated as coupled depth-dependent processes.

3.3 Retention and texture controls on SM-derived EM proxies

Retention controls were evaluated using station-level and station-season-level aggregation because retention variables such as TP, FC, WP, WHC, HWRpF4.2, and HWRpF6.2 are mainly station-static properties. These variables were related to SM and to the corresponding derived proxy variables at each depth, including ε_r, v, σ, α, and ρ_a. Because the EM variables are SM-derived, these relationships were interpreted as calibration-relevant associations showing how retention and texture condition the SM-to-EM translation, not as proof that independently measured EM behavior is caused by retention properties alone.

Linear association was quantified using Pearson's correlation coefficient (Pearson, 1895):

$$r_{xy} = \frac{\sum_{i=1}^{n}(x_i-\bar{x})(y_i-\bar{y})}{\sqrt{\sum_{i=1}^{n}(x_i-\bar{x})^2}\sqrt{\sum_{i=1}^{n}(y_i-\bar{y})^2}} \tag{7}$$

where r_{xy} is Pearson's correlation coefficient, x_i and y_i are paired observations, $\bar{x}$ and $\bar{y}$ are their means, and n is the number of paired observations.

https://doi.org/10.5194/essd-2026-563
Preprint. Discussion started: 23 September 2026

Monotonic association was quantified using Spearman's rank correlation coefficient (Spearman, 2010):

$$\rho_s = 1 - \frac{6\sum_{i=1}^{n} d_i^2}{n(n^2-1)} \qquad (8)$$

where ρ_s is Spearman's rank correlation coefficient, d_i is the difference between paired ranks, and n is the number of paired observations.

Linear and quadratic fits were screened to capture both direct and mildly nonlinear retention–HG responses. The quadratic model was expressed as:

$$\hat{y}_i = \beta_0 + \beta_1 x_i + \beta_2 x_i^2 \qquad (9)$$

where $\hat{y}_i$ is the fitted HG response, x_i is the HR predictor, and β_0, β_1, and β_2 are fitted regression coefficients.

Explained variance was evaluated using the coefficient of determination:

$$R^2 = 1 - \frac{\sum_{i=1}^{n}(y_i - \hat{y}_i)^2}{\sum_{i=1}^{n}(y_i - \bar{y})^2} \qquad (10)$$

where R^2 is the coefficient of determination, y_i is the observed value, $\hat{y}_i$ is the predicted value, $\bar{y}$ is the mean observed value, and n is the number of observations.

3.4 Integrated proxy indices and vertical buffering

Integrated profile-scale indices were calculated to summarize vertical buffering, EM propagation contrasts, and dielectric interface behavior in the proxy database. Dielectric contrasts between adjacent layers were expressed using the normal-incidence dielectric reflection coefficient:

$$R_{\varepsilon,z_1-z_2} = \frac{\sqrt{\varepsilon_{r,z_2}} - \sqrt{\varepsilon_{r,z_1}}}{\sqrt{\varepsilon_{r,z_2}} + \sqrt{\varepsilon_{r,z_1}}} \qquad (11)$$

where R_{ε,z_1-z_2} is the dielectric reflection coefficient between adjacent depths z_1 and z_2, and ε_{r,z_1} and ε_{r,z_2} are relative ε_r values at the two depths.

The Hydrogeo Buffering Index (HBI) was calculated as the coefficient of variation of ε_r across the 10–75 cm profile:

$$HBI = \frac{SD(\varepsilon_{r,10}, \varepsilon_{r,20}, \varepsilon_{r,30}, \varepsilon_{r,45}, \varepsilon_{r,60}, \varepsilon_{r,75})}{Mean(\varepsilon_{r,10}, \varepsilon_{r,20}, \varepsilon_{r,30}, \varepsilon_{r,45}, \varepsilon_{r,60}, \varepsilon_{r,75})} \qquad (12)$$

where SD is the standard deviation, $Mean$ is the arithmetic mean, and $\varepsilon_{r,z}$ is relative ε_r at depth z.

The EM Propagation Resistance Index ($EPRI$) was calculated as the profile-average α:

$$EPRI = Mean(\alpha_{10}, \alpha_{20}, \alpha_{30}, \alpha_{45}, \alpha_{60}, \alpha_{75}) \qquad (13)$$

https://doi.org/10.5194/essd-2026-563
Preprint. Discussion started: 23 September 2026

where α_z is the α proxy at depth z.

The Dielectric Attenuation Change Index (DA) was calculated between 10 and 75 cm as:

$$DA_{10-75} = \frac{\varepsilon_{r,10} - \varepsilon_{r,75}}{\varepsilon_{r,10}} \times 100 \qquad (14)$$

where DA_{10-75} is the dielectric attenuation change index, $\varepsilon_{r,10}$ is relative ε_r at 10 cm, and $\varepsilon_{r,75}$ is relative ε_r at 75 cm.

The Velocity Damping Index (VD) was calculated as:

$$VD_{10-75} = v_{75} - v_{10} \qquad (15)$$

where VD_{10-75} is the velocity damping index, v_{75} is EM wave velocity at 75 cm, and v_{10} is EM wave velocity at 10 cm.

The 10–75 cm ρ_a gradient was calculated as:

$$\nabla\rho_{a,10-75} = \frac{\rho_{a,75} - \rho_{a,10}}{0.65} \qquad (16)$$

where $\nabla\rho_{a,10-75}$ is the ρ_a gradient between 10 and 75 cm, $\rho_{a,75}$ and $\rho_{a,10}$ are ρ_a proxies at 75 and 10 cm, and 0.65m is the vertical distance between the two depths.

3.5 Spatial interpolation and national-scale mapping

Spatial organization of the SM-derived proxy variables was evaluated using station-level means of SM, ε_r, v, σ, α, and ρ_a. The station means were interpolated using inverse distance weighting (IDW), with a power parameter $p = 2$ and the nearest $k = 12$ stations. For each prediction location x_0, the interpolated value was calculated as (Shepard, 1968):

$$\hat{Z}(x_0) = \frac{\sum_{i=1}^{k} w_i(x_0) Z(x_i)}{\sum_{i=1}^{k} w_i(x_0)}, w_i(x_0) = \frac{1}{d(x_0, x_i)^p} \qquad (17)$$

where $\hat{Z}(x_0)$ is the interpolated value at location x_0, $Z(x_i)$ is the station value at location x_i, $w_i(x_0)$ is the distance-based weight, $d(x_0, x_i)$ is the distance between x_0 and x_i, p is the IDW power, and k is the number of nearest stations.

The interpolation grid was masked to the national boundary. Maps were produced for 10 and 75 cm to compare near-surface and deeper HG domains, while six-depth map products were retained as supporting outputs.

To synthesize the multi-parameter spatial patterns, an explainable 3D proxy state model was developed across the six measured horizons from 10 cm to 75 cm. A composite HG state index (HG state z) was calculated at station-depth scale from standardized SM, θ, S_w, ε_r, σ, α, WHC, FC, WP, and HWRpF4.2, with inverse contributions from v and log-transformed ρ_a. Thus, positive HG state z values represent higher-moisture, more retentive, more conductive, and more strongly dielectric proxy conditions, whereas negative values indicate lower-moisture,

https://doi.org/10.5194/essd-2026-563
Preprint. Discussion started: 23 September 2026

more resistive proxy conditions with faster expected EM propagation. The HG state z values and individual component variables were then interpolated using the same IDW settings and visualized as vertically separated depth slices to support spatial and depth-resolved interpretation.

3.6 Leakage-safe machine-learning analysis for calibration priors

A leakage-safe machine-learning analysis was used to evaluate whether hydraulic-retention and texture variables could predict the SM-derived EM proxy ranges without using SM or other derived proxy variables as predictors. Models were trained at the station-mean scale to match the station-static nature of the retention variables. The target variables were ε_r, v, σ, α, and ρ_a at each depth. Predictors were restricted to TP, FC, WP, WHC, HWR-pF4.2, HWR_pF6.2, grain-size fractions, and texture variables. For each model, the selected HG variable was used only as the response variable, while SM, θ, S_w, ε_r, v, ρ_a, σ, α, penetration terms, reflection terms, gradients, and other derived HG variables were excluded from the predictor matrix to avoid deterministic information leakage.

For positively skewed electrical targets, a logarithmic transformation was applied before model fitting:

$$y_i^* = \ln(1 + y_i) \qquad (18)$$

where y_i^* is the transformed target value and y_i is the original target value.

The models were trained using a deterministic 75/25 train–test split. Linear Regression, Random Forest, ExtraTrees, Gradient Boosting and HistGradientBoosting models (Friedman 2001; Geurts et al., 2006) were compared. Predictive performance was evaluated using R^2 from Eq. (19):

$$RMSE = \sqrt{\frac{1}{n}\sum_{i=1}^{n}(y_i - \hat{y}_i)^2}, \qquad MAE = \frac{1}{n}\sum_{i=1}^{n} | y_i - \hat{y}_i | \qquad (19)$$

where $RMSE$ is root mean square error, MAE is mean absolute error, y_i is the observed value, $\hat{y}_i$ is the predicted value, and n is the number of observations.

Feature importance was summarized across retained model–depth cases using the mean absolute model-specific contribution:

$$I_j = \frac{1}{N}\sum_{k=1}^{N} | \varphi_{jk} | \qquad (20)$$

https://doi.org/10.5194/essd-2026-563
Preprint. Discussion started: 23 September 2026

where I_j is the mean importance of predictor j, φ_{jk} is the model-specific contribution or importance value of predictor j in model–depth case k, and N is the number of retained model–depth cases.

The resulting model comparisons and feature-importance rankings were used to identify retention and texture variables that are useful as prior information for EM-to-SM calibration, while ensuring that predictive skill reflected independent retention and texture effects rather than circular dependence on the equations used to derive the proxy variables.

4. Results

4.1 Vertical organization of HG properties across the soil profile

The vertical HG profiles showed a coherent but moderate depth-dependent organization across the monitoring network (Fig. 3). Mean SM increased from 21.45% at 10 cm to 22.24–22.25% at 30–45 cm, equivalent to a 3.7–3.8% increase relative to the surface layer, before slightly decreasing to 22.05% at 75 cm (Fig. 3A). The narrow 95% CI values (±0.03–0.04%) reflect the large sample size and indicate that the vertical differences, although small in absolute magnitude, are systematic. This mid-profile SM maximum suggests that the 30–45 cm interval acts as a storage and buffering zone, where short-term atmospheric forcing is damped and retained water becomes more persistent.

As expected from the SM-to-EM proxy translation, ε_r followed the same vertical structure as SM, increasing from 11.72 at 10 cm to a maximum of 12.29 at 30 cm and remaining elevated at 45–75 cm (12.15–12.22; Fig. 3B). This represents a 4.8% increase from 10 to 30 cm, this indicates that the derived dielectric proxy primarily reflects retained water in the monitored profile. The inverse dielectric–velocity relationship was clearly expressed in the v profile (Fig. 3C). Mean v declined from 0.09546 m ns^{-1} at 10 cm to 0.09351 m ns^{-1} at 45 cm, a 2.0% reduction, before increasing slightly to 0.09455 m ns^{-1} at 75 cm. Although the absolute variation was small, the velocity minimum coincided with the SM and ε_r maximum, showing that the moisture-retentive mid-profile layers slow EM propagation through increased dielectric polarization.

Electrical properties showed a stronger vertical contrast than SM and ε_r. Mean σ increased from 0.00399 S m^{-1} at 10 cm to 0.00428 S m^{-1} at 30 cm, corresponding to a 7.4% increase, and then remained slightly lower but still elevated at 45–75 cm (0.00416–0.00425 S m^{-1}; Fig. 3D). In contrast, ρ_a decreased from 586.53 Ω m at 10 cm to 545.16 Ω m at 45 cm, a 7.1% reduction,

https://doi.org/10.5194/essd-2026-563
Preprint. Discussion started: 23 September 2026

before rising to 606.16 Ω m at 75 cm (Fig. 3E). This reciprocal σ–ρa behavior indicates stronger conductive continuity in the middle profile, most likely associated with higher water retention and improved pore-water connectivity.

α showed the clearest damping response to the mid-profile HG maximum (Fig. 3F). Mean α increased from 0.00180 m^{-1} at 10 cm to 0.00189 m^{-1} at 30 cm, a 4.9% increase, and then gradually declined to 0.00184 m^{-1} at 75 cm. The co-occurrence of measured higher SM with derived higher ε_r, σ, and α and lower v and ρ_a identifies the 30-45 cm interval as the main proxy transition zone of the profile. It was noticed that the vertical structure indicates that HG behavior is not controlled by SM alone, but by the coupled effect of water storage, dielectric polarization, conductive pathways, and depth-dependent retention architecture.

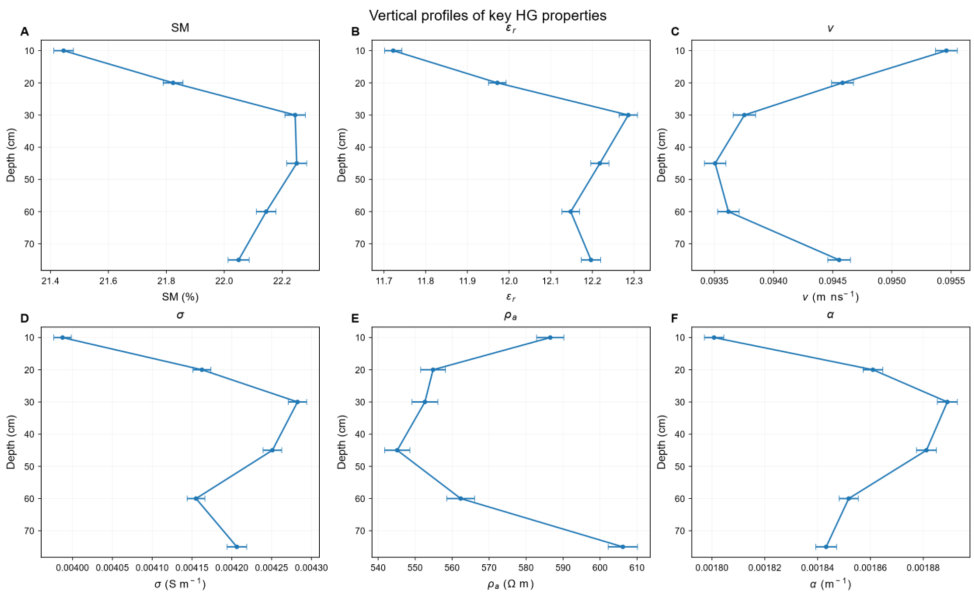

Fig. 3. Vertical profiles of key HG properties across the soil profile. Points show mean values and horizontal bars indicate 95% CI for SM (A), ε_r (B), v (C), σ (D), ρa (E), and α (F).

4.2 Texture-dependent HG differentiation

Texture exerted a first-order control on measured SM and the corresponding SM-derived EM proxy across the soil profile (Figs. 4–5). Among the 117 stations, fine loam was the dominant texture class (59.5%), followed by sandy soil (16.4%), coarse loam (13.8%), and clayey soil (10.3%). Seasonal–depth HG patterns (Fig. 4A–F) show a consistent coupling between

https://doi.org/10.5194/essd-2026-563
Preprint. Discussion started: 23 September 2026

hydraulic retention and EM response. Winter and spring were characterized by higher SM (Fig. 4A), ε_r (Fig. 4B), σ (Fig. 4E), and α (Fig. 4F), accompanied by lower v (Fig. 4C) and ρ_a (Fig. 4D). In contrast, summer exhibited reduced SM and ε_r together with increased v and ρ_a, reflecting lower-moisture conditions and reduced dielectric polarization. Across all seasons, SM increased from ~18–19% near the surface to ~20–21% at 75 cm, while ε_r increased from ~9–10 to ~12–15, whereas v decreased from ~0.103 to ~0.085 m ns^{-1}, indicating progressively stronger water storage and EM damping with depth. The corresponding standardized anomaly patterns (Fig. A1) confirm that these seasonal contrasts are persistent throughout the 10–75 cm profile.

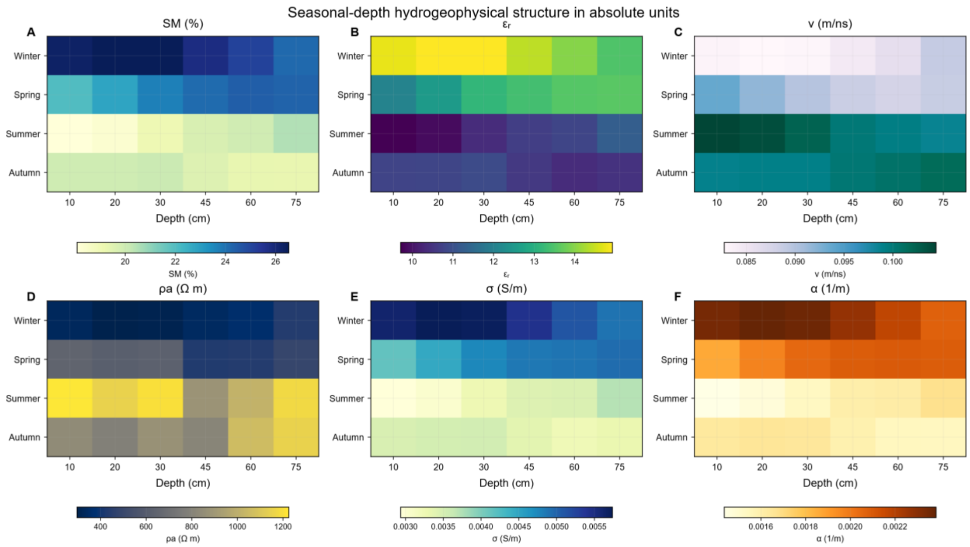

Fig. 4. Seasonal–depth HG structure across the soil profile. Heatmaps show mean (A) SM, (B) ε_r, (C) v, (D) ρ_a, (E) σ, and (F) α for four seasons and six depths (10–75 cm). Winter and spring exhibit higher SM, ε_r, σ, and α and lower v and ρ_a than summer. Increasing depth is generally associated with higher SM, ε_r, σ, and α and lower v, indicating stronger WS and EM damping in deeper layers.

Texture-specific distributions further demonstrate the dominant role of soil texture in controlling HG behavior (Fig. 5). Across all depths, sandy soils consistently exhibited the lowest SM and ε_r and the highest v and ρ_a (Fig. 5A–X), indicating limited WHC and efficient EM transmission. Mean SM averaged 13.9% (13.1–14.7%), ε_r averaged 7.65 (7.19–8.16), v averaged 0.119 m ns^{-1} (0.116–0.121 m ns^{-1}), and ρ_a reached 1793 Ω m, with maximum values exceeding 2000 Ω m. In contrast, clayey soils displayed the strongest moisture-retentive

https://doi.org/10.5194/essd-2026-563
Preprint. Discussion started: 23 September 2026

response, with SM reaching 27.3%, ε_r increasing to 15.55, v decreasing to 0.081 m ns^{-1}, and ρ_a declining to 475 Ω m. Relative to sandy soils, clayey soils showed nearly double SM and ε_r, a 31% reduction in v, and a 74% reduction in ρ_a, reflecting enhanced dielectric polarization and electrical conduction.

Fine loam exhibited a similar but slightly weaker response than clayey soils, with SM = 24.5%, ε_r = 13.50, v = 0.087 m ns^{-1}, and the highest α (0.00211 m^{-1}), approximately 76% greater than in sandy soils. Coarse loam occupied an intermediate position (SM = 19.1%, ε_r = 10.02, v = 0.100 m ns^{-1}, ρ_a = 689 Ω m), indicating moderate hydraulic retention and dielectric response. Importantly, the texture ranking remained nearly unchanged from 10 to 75 cm (Fig. 5A–X), demonstrating that texture exerts a stronger control on HG properties than depth alone.

Texture-dependent indices further reinforced these contrasts. The $EPRI$ increased from 0.00112 m^{-1} in sandy soils to 0.00157 m^{-1} in coarse loam, 0.00184 m^{-1} in clayey soils, and 0.00208 m^{-1} in fine loam, representing an 86% increase relative to sandy soils. Vertical dielectric behavior was also texture-specific: coarse loam showed a positive dielectric change between 10 and 75 cm (+13.1%), whereas clayey soil (−10.9%), fine loam (−5.5%), and sandy soil (−9.9%) exhibited net decreases. Reflection coefficients indicated the strongest positive dielectric impedance contrast in clayey soils between 10 and 20 cm (R = 0.023) and the strongest negative contrast in coarse loam between 60 and 75 cm (R = −0.024), while fine loam remained close to zero, indicating smoother dielectric transitions and greater hydraulic continuity.

https://doi.org/10.5194/essd-2026-563
Preprint. Discussion started: 23 September 2026

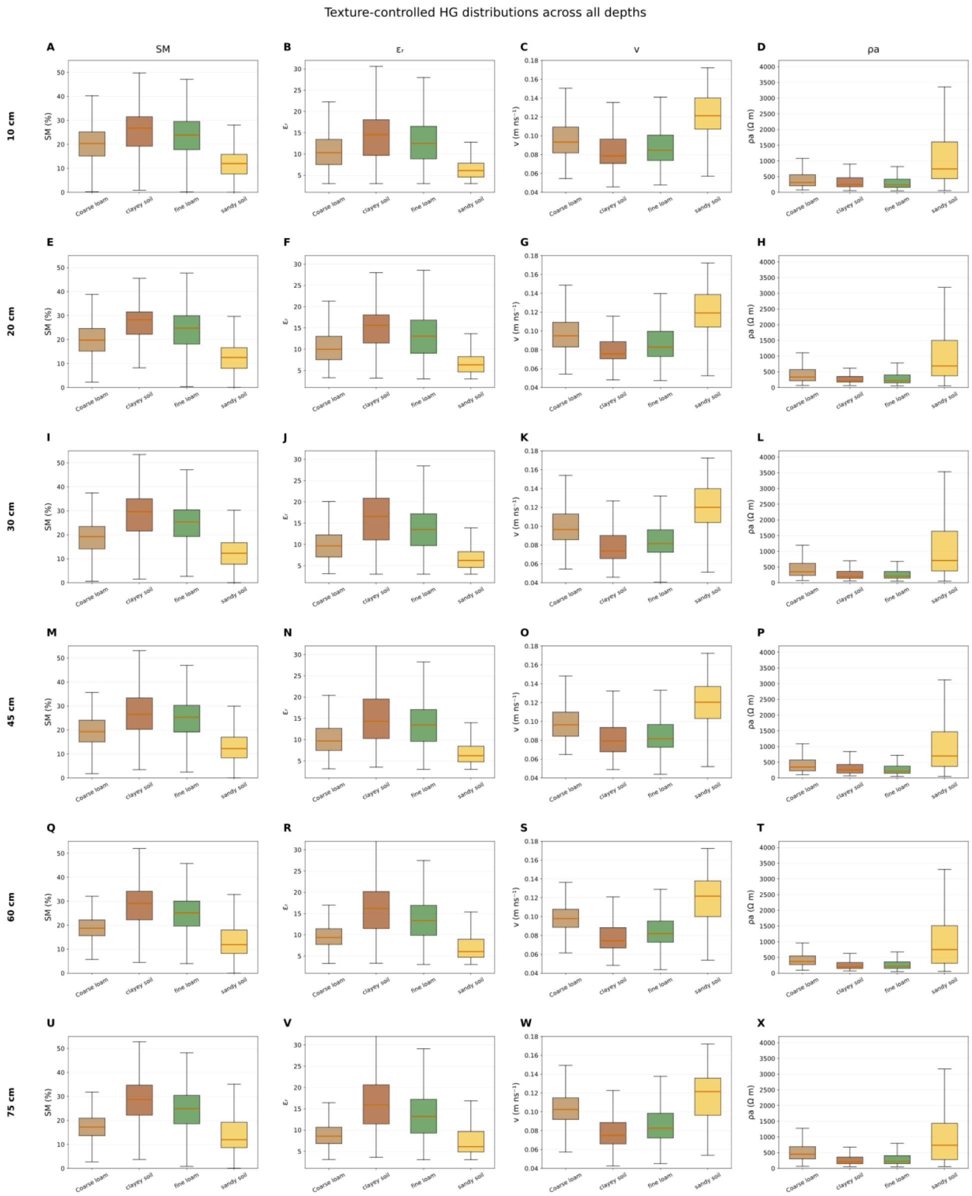

Fig. 5. Texture-controlled distributions of HG properties across six depths (10–75 cm). Boxplots show SM (A, E, I, M, Q, U), ε_r (B, F, J, N, R, V), v (C, G, K, O, S, W), and ρ_a (D, H, L, P, T, X) for coarse loam, clayey soil, fine loam, and sandy soil. Texture-specific differences persist throughout the profile, with clayey and fine-loam soils characterized by higher SM and ε_r and lower v and ρ_a, whereas sandy soils exhibit the opposite behavior.

https://doi.org/10.5194/essd-2026-563
Preprint. Discussion started: 23 September 2026

4.3 Retention controls on SM-derived EM proxy ranges

The texture-dependent HG contrasts were further explained by the strong influence of HR properties. HG–hydraulic relationships were evaluated using Pearson (r), Spearman (ρ), and R^2 to capture linear association, monotonic consistency, and explained variance, respectively. Across all investigated depths, the strongest relationships consistently involved WHC, followed by WP and, to a lesser extent, HWR4.2 and HWR6.2, indicating that HR variables explain variation in SM-derived proxy variables because they describe water-storage capacity.

Among all tested relationships, WHC emerged as the dominant predictor of both dielectric and propagation properties. The strongest relationship was observed between WHC_{60} and v_{60}, which exhibited a Pearson correlation of $r = -0.888$ and a quadratic fit of $R^2 = 0.792$. Similarly strong relationships were observed between WHC_{30} and v_{30} ($r = -0.860$, $R^2 = 0.747$) and between WHC_{75} and v_{75} ($r = -0.86$, $R^2 = 0.75$) (**see Table 1**). These results demonstrate that increasing water-holding capacity systematically reduces v, confirming that retained water enhances dielectric polarization and slows wave propagation.

Table 1. Strongest retention controls on SM-derived EM proxy ranges across the soil profile. Relationships are shown for station-scale means ($n = 117$) using r, ρ, and maximum R^2 from the tested linear and quadratic fits. WHC was the dominant retention variable controlling SM, ε_r, and v, with positive associations for SM, ε_r, σ, and α, and inverse associations for v and ρ_a.

HG variable	Depth (cm)	HR variables	r	ρ	Maximum R^2
ε_r	60	WHC_{60}	0.850	0.843	0.769
SM	60	WHC_{60}	0.878	0.830	0.781
v	60	WHC_{60}	−0.888	−0.812	0.792
v	75	WHC_{75}	−0.860	−0.835	0.742
SM	75	WHC_{75}	0.840	0.842	0.715
ε_r	75	WHC_{75}	0.804	0.848	0.687
SM	30	WHC_{30}	0.851	0.774	0.729
v	30	WHC_{30}	−0.860	−0.754	0.747
ε_r	30	WHC_{30}	0.824	0.791	0.710
σ	60	WHC_{60}	0.772	0.772	0.632
α	60	WHC_{60}	0.766	0.719	0.589

https://doi.org/10.5194/essd-2026-563
Preprint. Discussion started: 23 September 2026

ρa	60	HWR_{60} (pF 4.2)	−0.755	−0.728	0.644

The response of ε_r showed an opposite of v but equally strong pattern. WHC_{60} explained a substantial proportion of the variability in ε_{r60} (ρ = 0.84, R^2 = 0.77), while similarly strong relationships occurred at 30 cm (ρ = 0.79, R^2 = 0.71) and 75 cm (ρ = 0.80, R^2 = 0.61). These findings indicate that soils with greater water-storage capacity consistently exhibit higher ε_r because a larger fraction of pore space remains occupied by electrically polarizable water (Fig. 6; Fig. A3; Table A1).

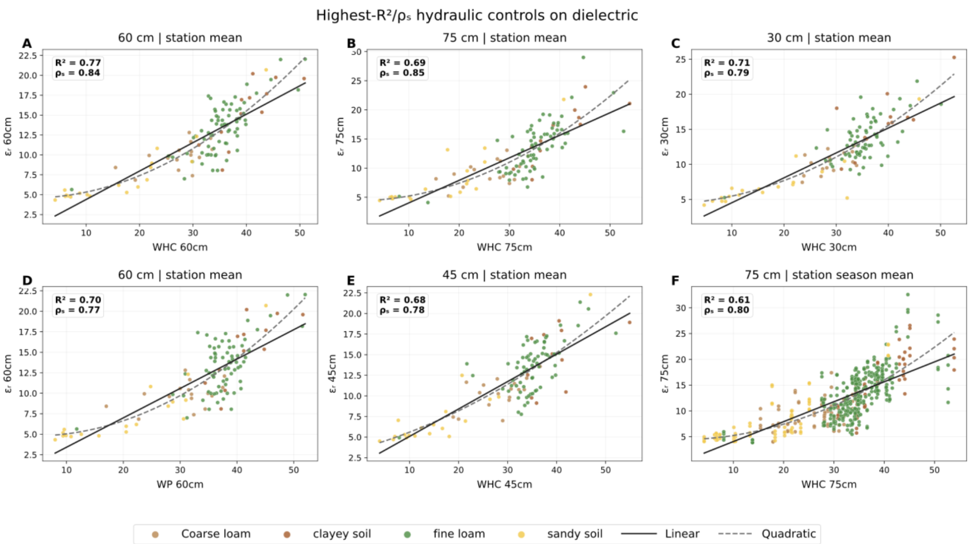

Fig. 6. Examples of the strongest HR controls on ε_r behavior across the soil profile. Panels A–F show representative relationships between retention properties (WHC and WP) and ε_r at selected depths and aggregation scales. Points are colored by texture class, while solid and dashed lines represent linear and quadratic fits, respectively.

HR properties also strongly controlled soil moisture itself. Relationships between WHC and SM reached r = 0.878 (R^2 = 0.78) at 60 cm, r = 0.851 (R^2 = 0.729) at 30 cm, r = 0.839 (R^2 = 0.715) at 75 cm, and r = 0.839 (R^2 = 0.704) at 45 cm. These values demonstrate that HR metrics are not merely correlated with HG variables but directly regulate the long-term moisture storage conditions that govern EM behavior (Fig. A3).

A similar pattern was observed for WP. At 60 cm depth, WP_{60} showed strong relationships with v_{60} (r = −0.860, R^2 = 0.742), SM_{60} (r = 0.839, R^2 = 0.716), and ε_{r60} (r = 0.806, R^2 = 0.695). The

https://doi.org/10.5194/essd-2026-563
Preprint. Discussion started: 23 September 2026

persistence of these relationships suggests that not only plant-available water storage but also strongly retained water contributes substantially to dielectric behavior and EM damping (Fig. A2; Fig. A3).

The influence of strongly bound water became increasingly evident through the HWR variables. For example, $HWR6.2_{60}$ exhibited a strong positive relationship with ε_{r60} ($r = 0.782$, $R^2 = 0.624$), while $HWR4.2_{45}$ showed strong relationships with SM_{45} ($r = 0.782$, $R^2 = 0.665$) and ε_{r45} ($r = 0.796$, $R^2 = 0.654$). These results indicate that hygroscopically retained water continues to influence dielectric properties even under relatively low soil-moisture conditions, highlighting the importance of bound-water fractions in controlling EM responses.

σ displayed comparable behavior. The strongest σ relationship was observed between WHC_{60} and σ_{60} ($r = 0.772$, $R^2 = 0.632$), demonstrating that increased water retention enhances conductive pathways and facilitates charge transport through the soil matrix. This increase in σ is consistent with the higher α and lower resistivity observed in fine-textured and moisture-retentive soils (Table A1).

4.4 Integrated HG indices and vertical buffering

Integrated HG indices revealed clear texture-dependent differences in vertical EM propagation and moisture redistribution (Fig. 7). The HBI showed relatively similar median values (~0.16–0.19) across texture groups but broader interquartile ranges and higher upper extremes in fine loam and clayey soils, indicating greater capacity to dampen vertical moisture fluctuations and maintain hydraulic stability throughout the profile (Fig. 7A).

The $EPRI$ increased from sandy soils (median ≈ 0.0010) to coarse loam (0.0015), clayey soil (0.0019), and fine loam (0.0021), indicating that EM transmission resistance was approximately 90–110% greater in fine-textured soils than in sandy soils (Fig. 7B). This pattern reflects stronger dielectric losses associated with higher water-retention capacity.

The VD ranged from approximately −0.06 to +0.06 m ns^{-1}. Coarse loam exhibited the highest median damping (~+0.008 m ns^{-1}), while the remaining texture groups clustered around zero. Positive damping values indicate stronger reductions in v with depth and therefore greater downward moisture accumulation (Fig. 7C).

The $\nabla\rho$ Index displayed the greatest variability of all integrated metrics. Sandy soils showed an exceptionally wide range (−3300 to +2800 Ω m), whereas clayey soil and fine loam remained

https://doi.org/10.5194/essd-2026-563
Preprint. Discussion started: 23 September 2026

centered near zero with substantially narrower distributions. This indicates markedly stronger vertical electrical contrasts and greater moisture heterogeneity in sandy profiles (Fig. 7D).

The DA exhibited substantial variability, ranging from approximately −115% to +85%. Coarse loam displayed the highest median value (~+15%), whereas clayey soil, fine loam, and sandy soil remained near zero or slightly negative. This suggests increasing dielectric energy dissipation with depth in coarse-loam profiles, consistent with enhanced subsurface moisture storage (Fig. 7E).

Rε remained generally small ($|R| < 0.03$), indicating predominantly gradual dielectric transitions between adjacent horizons. Fine-loam soils exhibited the most uniform dielectric structure, whereas clayey soils showed the largest positive and negative coefficients (~+0.023 to −0.025), reflecting stronger hydraulic discontinuities and sharper dielectric contrasts between layers. Additional depth-specific Rε patterns are shown in Fig. A2, confirming that dielectric interface contrasts were strongest in clayey soils at 10–20 cm and in coarse-loam soils at 60–75 cm (Fig. 7F).

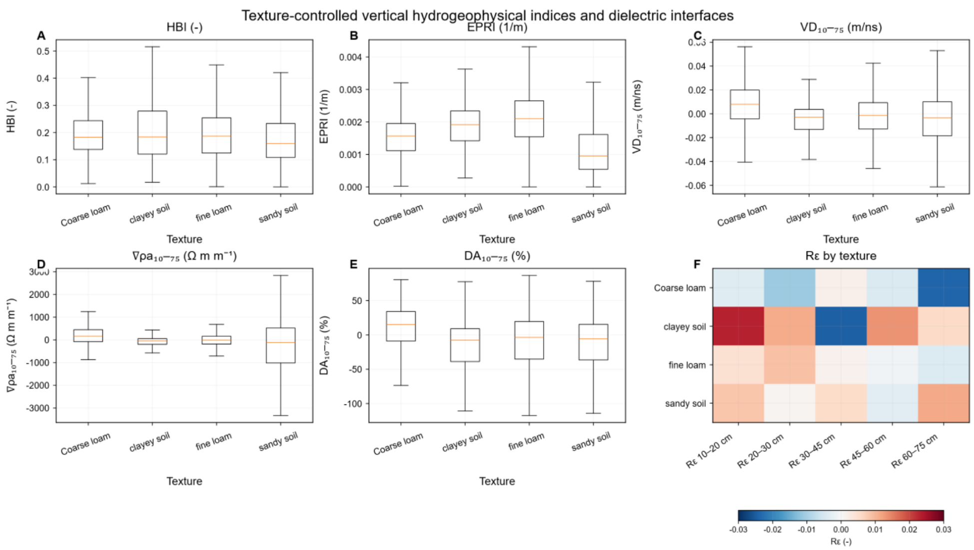

Figure 7. Texture-controlled variation in integrated HG indices and dielectric interfaces. Boxplots show the distributions of HBI (A), EPRI (B), VD_{10-75} (C), $\nabla\rho a_{10-75}$ (D), and DA_{10-75} (E) across texture classes, while panel F illustrates depth-specific dielectric reflection coefficients (Rε). Positive and negative values indicate the direction of vertical HG change and dielectric impedance contrasts between adjacent layers.

https://doi.org/10.5194/essd-2026-563
Preprint. Discussion started: 23 September 2026

The integrated indices showed that fine-textured soils possess stronger HG buffering, higher expected EM propagation resistance based on the derived proxy, and more stable vertical dielectric organization, whereas sandy soils are characterized by weaker buffering and substantially greater vertical electrical heterogeneity. These results provide a quantitative process-based link between hydraulic retention and EM behavior across contrasting soil environments.

4.5 Spatial Organization and Explainable 3D SM-to-EM proxy State Model Across Hungary

The IDW maps (Fig. 8) revealed coherent regional-scale HG domains across Hungary, demonstrating that the vertical, textural, and HR relationships identified in the previous sections are spatially organized rather than randomly distributed. Across the 10-75 cm profile, the central Danube-Tisza Interfluve consistently formed a moisture-deficient and resistive HG domain, characterized by low SM (<15-18%), low ε_r (<8-10), low σ (<0.002-0.003 S m^{-1}), and low α (<0.0012-0.0015 m^{-1}), but high v (v > 0.10-0.12 m ns^{-1}) and ρa (ρ_a > 1,500-2,000 Ω m). In contrast, northeastern, eastern, and northwestern Hungary formed higher-moisture and more retentive HG domains, where higher SM (>26-30%), ε_r (>14-18), σ (>0.005-0.007 S m^{-1}), and α (>0.0022-0.0028 m^{-1}) coincided with lower v (<0.08-0.09 m ns^{-1}) and ρa (<300-600 Ω m). This reciprocal spatial organization indicates strong coupling among water storage, dielectric polarization, conductive pore-water connectivity, EM attenuation, and resistive behavior.

The near-surface and deeper maps (Fig. 8) showed that these HG domains persist from 10 to 75 cm, but with stronger contrasts at depth. Moisture-rich regions exhibited elevated ε_r and σ together with reduced v and ρ_a, confirming that retained water increases dielectric polarization and conductive connectivity while slowing EM propagation. Conversely, the central moisture-deficient belt maintained lower ε_r, σ, and α and higher v and ρa, indicating limited pore-water connectivity and stronger resistive behavior. The σ-ρa contrast became increasingly pronounced below 45 cm, suggesting that deeper HG organization is controlled more strongly by subsurface HR architecture than by short-term surface moisture variability.

https://doi.org/10.5194/essd-2026-563
Preprint. Discussion started: 23 September 2026

Open Access Earth System Science Data Discussions

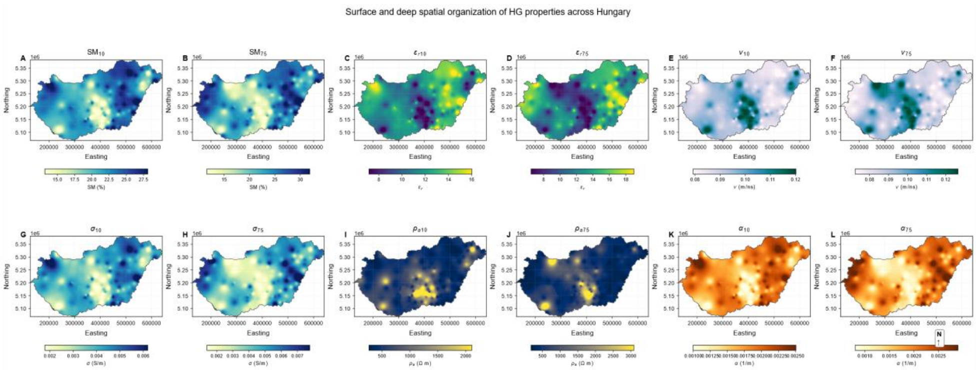

Fig. 8. Spatial organization of HG properties across Hungary derived from IDW interpolation. Surface (10 cm) and deep (75 cm) maps are shown for (A–B) SM, (C–D) ε_r, (E–F) v, (G–H) σ, (I–J) ρa, and (K–L) α. Consistent spatial gradients are evident across all variables, with a central moisture-deficient domain characterized by low SM, ε_r, σ, and α and high v and ρa, contrasting with moisture-rich northeastern, eastern, and northwestern regions. These patterns become more pronounced at 75 cm, indicating stronger subsurface hydraulic control.

The explainable 3D proxy state model (Fig. 9; interactive version: interactive 3D model) provides a depth-resolved synthesis of the coupled soil-water-EM system across the 10-75 cm root zone. Unlike individual IDW maps of SM, ε_r, v, σ, ρa, and α, the model integrates water-content variables, HR properties, and EM responses into a composite HG state index (HG state z). Positive HG state z values indicate higher-moisture, more retentive, and more EM lossy conditions, where high SM, θ, S_w, ε_r, σ, α, WHC, FC, WP, and HWRpF4.2 coincide with reduced v and ρ_a. Negative values indicate lower-moisture, more resistive, and more transmissive conditions, where reduced water storage and dielectric polarization coincide with faster EM propagation and higher ρ_a.

Physically, HG state z captures the joint expression of pore-water storage, retention capacity, dielectric polarization, conductive pore-water connectivity, EM damping, and resistive behavior rather than soil moisture alone. Across the dataset, the component variables spanned broad HG contrasts: SM = 5.8-43.9%, ε_r = 4.09-29.00, v = 0.057-0.149 m ns^{-1}, σ = 0.00028-0.01383 S m^{-1}, ρ_a = 94-12,441 Ω m, and α = 0.00023-0.00428 m^{-1}. The model therefore captures the transition from low-moisture, resistive domains to high-moisture, retentive, dielectric-conductive domains.

https://doi.org/10.5194/essd-2026-563
Preprint. Discussion started: 23 September 2026

The 3D structure confirms that proxy provinces are vertically persistent rather than surface-limited. High-state domains remain coherent across several horizons in eastern, northeastern, and northwestern Hungary, indicating stronger water storage, higher retention capacity, and enhanced pore-water connectivity. Conversely, low-state domains persist across the central Danube-Tisza Interfluve, where lower SM, ε_r, σ, and α coincide with higher v and ρ_a. This persistence shows that national HG organization is controlled not only by instantaneous moisture, but by deeper HR architecture. The 30-45 cm interval emerges as the dominant transition and buffering zone, where retained water most strongly modulates dielectric, conductive, α, v, and resistivity responses. Thus, the explainable 3D model provides a mechanistic bridge between station-scale measurements, vertical hydraulic retention, and national-scale calibration provinces.

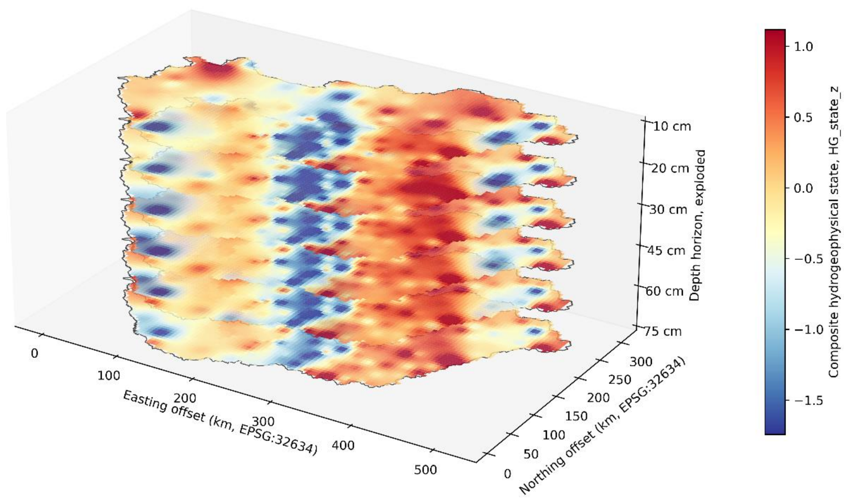

Fig. 9. Explainable 3D proxy state model of the Hungarian DWMS root-zone profile. Six vertically separated slices represent the measured 10, 20, 30, 45, 60, and 75 cm horizons. Colors show the composite HG state z index, integrating SM, θ, S_w, ε_r, σ, α, WHC, FC, WP, HWRpF4.2, inverse v, and inverse log-transformed ρa. An interactive version is available here interactive 3D model.

4.6 HR controls on SM-derived EM proxy ranges

HR properties exerted strong control on HG behavior across the entire soil profile, as demonstrated by both direct correlation analysis and machine-learning predictions (Figs. 10–11). WHC showed the strongest and most consistent relationships with HG properties,

https://doi.org/10.5194/essd-2026-563
Preprint. Discussion started: 23 September 2026

Open Access Earth System Science Data Discussions

explaining substantial proportions of the variance in ε_r, v, and σ responses across all depths (Fig. 10A–C). ε_r increased systematically with WHC ($R^2 = 0.62$–0.77; $\rho = 0.72$–0.85), whereas v decreased with increasing WHC ($R^2 = 0.68$–0.79; $\rho = -0.68$ to -0.84). Σ exhibited similarly strong positive relationships ($R^2 = 0.61$–0.63; $\rho = 0.74$–0.77), confirming that retained water acts as the primary regulator of dielectric polarization, EM-wave propagation, and electrical conduction.

Machine-learning models further demonstrated that predictive control strengthened with depth. v and ε_r were the most predictable HG variables, achieving R^2 values of 0.75–0.83 and 0.68–0.81, respectively (Appendix A; Figs. A4–A5). v increased from $R^2 = 0.78$ at 10 cm to 0.83 at 60–75 cm, whereas ε_r reached maximum performance at 75 cm ($R^2 = 0.81$). The limited variation in predictive skill across depths ($\Delta R^2 \approx 0.08$–0.13) indicates stable hydraulic control throughout the profile.

ε_r and α showed slightly lower but similarly robust predictability. ε_r increased from $R^2 = 0.62$ at 10 cm to 0.76 at 60 cm, while α increased from 0.63 to 0.75 between the same depths (Appendix A; Figs. A6–A7). This ~20–23% improvement with depth suggests that conductive and α processes become increasingly controlled by intrinsic HR properties and less influenced by short-term atmospheric forcing.

The strongest depth dependence was observed for ρ_a. Prediction skill remained relatively modest in shallow layers ($R^2 = 0.30$–0.56 at 10–30 cm) but increased sharply below 45 cm, reaching $R^2 = 0.66$ at 45 cm, 0.86 at 60 cm, and 0.85 at 75 cm. Consequently, resistivity exhibited the largest vertical gain in predictive performance (>0.55 R^2 units), indicating that deeper resistivity is predominantly governed by long-term water-storage characteristics, whereas shallow resistivity is influenced by additional transient environmental controls. Therefore, across all HG properties, predictive performance ranked: v ($R^2 = 0.75$–0.83) ≈ ε_r (0.68–0.81) > σ (0.62–0.76) ≈ α (0.63–0.75) > ρ_a (0.30–0.86).

https://doi.org/10.5194/essd-2026-563
Preprint. Discussion started: 23 September 2026

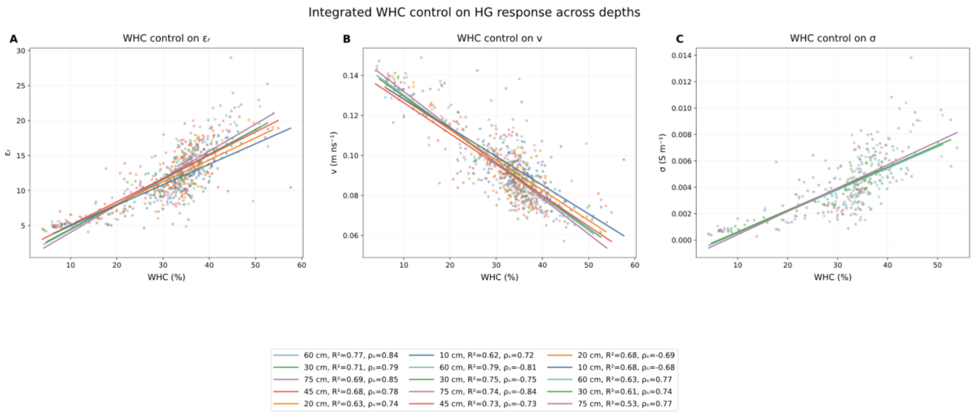

Fig. 10 Integrated WHC control on HG response across depths. Relationships between WHC and (A) ε_r, (B) v, and (C) σ. Colored trendlines represent individual depths (10–75 cm). Strong positive relationships were observed for ε_r and σ, whereas v decreased with increasing WHC. The strength of the relationships generally increased with depth, indicating progressively stronger HR control in deeper soil layers.

Feature-importance (FI) analysis revealed a remarkably consistent control structure (Fig. 11A–E). WHC was the dominant predictor for ε_r, v, σ, and α, with mean importance values reaching approximately 0.09–0.13 at 60–75 cm. WP represented the second most influential predictor group, whereas HWR parameters (particularly pF4.2–pF6.2) became increasingly important for resistivity prediction. For ρ_a, HWR30cm pF4.2 was the strongest individual predictor (importance ≈ 0.10), followed by WP75cm and WHC60cm (Fig. 11E). The repeated dominance of WHC, WP, and HWR variables demonstrates that HG behavior is governed primarily by soil water-storage and retention characteristics rather than texture alone.

https://doi.org/10.5194/essd-2026-563
Preprint. Discussion started: 23 September 2026

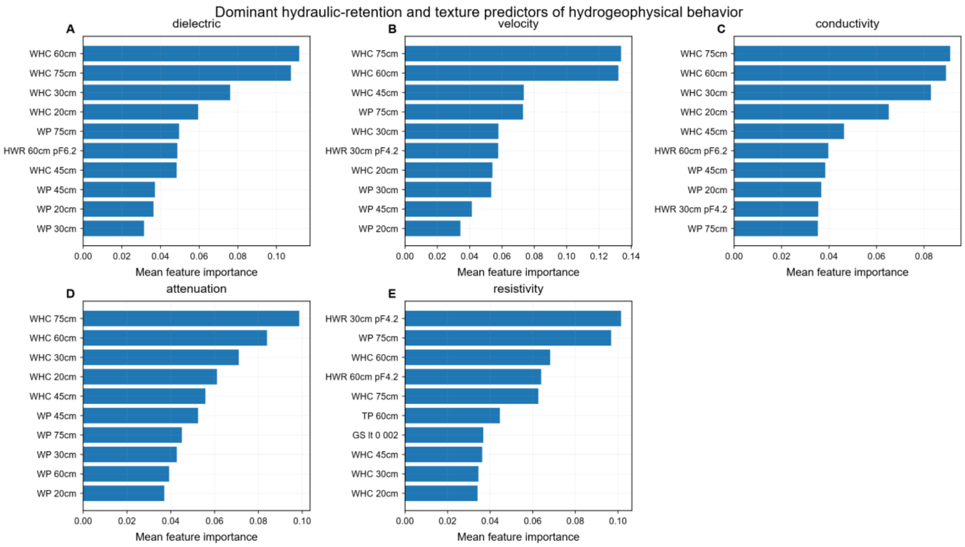

Fig. 11. Dominant HR and texture predictors of HG behavior. Mean FI from retention-only ML models for (A) ε_r, (B) v, (C) σ, (D) α, and (E) ρa. WHC was the dominant predictor for ε_r, v, σ, and α, whereas HWR and WP contributed more strongly to ρ_a prediction.

Among the evaluated algorithms, ExtraTrees and RandomForest consistently provided the highest and most stable predictive performance across depths and HG variables, particularly for ε_r, v, σ, and α, while Gradient Boosting produced the highest resistivity prediction skill ($R^2 \approx 0.91$ at 60 cm). This pattern indicates that non-linear ensemble methods are most effective for capturing retention-driven HG responses and their depth-dependent variability.

5. Discussion

5.1. Vertical organization of measured SM and derived EM proxy variables

The present study revealed a coherent vertical organization of measured SM and derived EM proxy variables, with the 30–45 cm interval acting as the main mid-profile storage and buffering zone. Mean SM increased from 21.45% at 10 cm to 22.24–22.25% at 30–45 cm, then slightly declined to 22.05% at 75 cm. This was mirrored by ε_r, which rose from 11.72 to 12.29, while v decreased from 0.09546 to 0.09351 m ns^{-1} and ρ_a declined from 586.5 to 545.2 Ω m by 45 cm. Because ε_r, v, σ, α, and ρ_a were derived from SM, this coupled pattern should be interpreted as the expected SM-to-EM proxy translation, not as independent geophysical validation. This behavior is also consistent with the broader vadose-zone measurement framework of Vereecken et al. (2008), who emphasized that SM observations are most powerful when interpreted as part

https://doi.org/10.5194/essd-2026-563
Preprint. Discussion started: 23 September 2026

of a coupled hydrological state system, and with Topp et al. (1980) and Huisman et al. (2003), who established the dielectric basis for translating water-content variation into EM response. Cao et al. (2020) reported strong dielectric–VSWC relationships, with the best GPR-based prediction for the 0–40 cm layer ($R^2 = 0.725$; RMSE = 0.027 $m^3\ m^{-3}$), and showed that rainfall-related VSWC increases were most pronounced in the 20–40 cm interval. Similarly, Yu et al. (2026) showed that infiltration-induced increases in near-surface permittivity create low-v guided-wave behavior sensitive to vertical SWC redistribution, while Yu et al. (2022) demonstrated that coupled GPR inversion can recover layer thickness and hydraulic parameters. These studies do not identify the exact 30–45 cm zone found here, but they strongly support the same mechanism: vertical water redistribution produces higher ε_r and lower v. The present six-depth result extends those GPR-based interpretations by identifying a persistent national-scale mid-profile proxy buffering zone that can guide future GPR and resistivity calibration, rather than only event-scale wetting-front redistribution (Steelman et al., 2012; Cheng et al., 2023).

The inverse ρ_a response and parallel increase in σ and α also agree with integrated ERT–GPR and petrophysical studies. Zou et al. (2023) showed that infiltration causes decreasing electrical resistivity and increasing dielectric constant, enabling the wetting front and moisture redistribution to be monitored, while Abbas et al. (2022) found very good correspondence between electrical resistivity, relative ε_r and water-content distributions along a vertically heterogeneous vadose-zone profile. This agrees with earlier AGU evidence that time-lapse ERT can resolve three-dimensional and temporal variation in soil water content (Zhou et al., 2001) and that resistivity information can identify layered vadose-zone structure when interpreted hydrogeophysically (Tartakovsky et al., 2008). Sun et al. (2020) further showed that resistivity-derived soil water estimates depend strongly on texture, land use, depth and high- and low-moisture states, supporting our interpretation that the mid-profile HG maximum reflects retention architecture rather than SM alone. This interpretation is also consistent with Moghadas and Badorreck (2019), who emphasized the nonlinear σ–θ relationship, and with Kozma et al. (2024) and Yosef et al. (2026), who highlighted the importance of local hydraulic parametrization, vertical discretization, soil depth and clay-related controls in soil-water modelling. Conceptually, the result follows Grayson et al. (1997), who described switches between vertically controlled low-moisture states and laterally connected high-moisture states. Time-lapse electrical resistivity monitoring has also shown that resistivity changes can record coupled soil-water and solute/groundwater dynamics, although interpretation remains sensitive to salinity and pore-water σ (Hayley et al., 2009). Thus, the 30–45 cm proxy buffering zone

https://doi.org/10.5194/essd-2026-563
Preprint. Discussion started: 23 September 2026

reflects how water storage, pore connectivity, dielectric translation, conductive pathways and depth-dependent HR structure combine to shape the expected EM response, rather than providing independent evidence of measured EM behavior. To place these findings in the context of previous HG research, **Table 2** compares the main quantitative results of the present study with published GPR, ERT, dielectric, soil-water and modelling studies.

Table 2. Table 2. Quantitative comparison of the present SM-derived proxy results with published studies. The table contrasts the main findings of this study, including the 30-45 cm proxy buffering zone, SM-ε_r-v-ρa translation, retention and texture effects, spatial proxy provinces, and explainable 3D proxy representation, with comparable results from previous GPR, ERT, dielectric, soil-water and modelling studies.

Comparison theme	Present study result	Published benchmark	Comparison	Scientific meaning
Vertical HG buffering zone	Persistent 30-45 cm zone: SM = 22.24-22.25%, ε_r = 12.29, v = 0.09351 m ns^{-1}, ρ_a = 545.2 Ω m.	Cao et al. (2020): strongest GPR-VSWC performance for 0-40 cm, RMSE = 0.027 m³ m^{-3} and R^2 = 0.725.	Similar mechanism, more specific vertical diagnosis	Both identify upper-root-zone sensitivity, but this study isolates a persistent national 30-45 cm HG buffering horizon rather than an event-scale field response.
ε_r/ v predictability	Leakage-safe ML reached R^2 = 0.68-0.81 for ε_r and R^2 = 0.75-0.83 for v.	Cao et al. (2020): GPR-derived VSWC prediction at R^2 = 0.725 for the best 0-40 cm model.	Similar to higher predictive strength	The retention-constrained framework achieves comparable or stronger skill while predicting HG behavior across six depths and national stations.
HR control	WHC relationships reached R^2 = 0.62-0.79 and Spearman ρ = 0.72-0.85 for ε_r, v, σ and SM.	Finkenbiner et al. (2019): CRNP + EOF HG information reduced field-capacity RMSE by 20-25%.	Stronger mechanistic quantification	Both show that HG data improve hydraulic-property inference; this study directly quantifies WHC as a depth-dependent control on EM properties.
Hydraulic model performance	Retention predictors produced high skill for v, ε_r and deeper ρ_a, with ρ_a reaching $R^2 \approx$ 0.86 at 60-75 cm.	Kozma et al. (2024): calibrated soil-moisture simulation NSME = 0.50, 0.54 and 0.71 at Hungarian sites.	Higher statistical skill for HG targets	Although targets differ, retention properties explain EM behavior strongly, especially in deeper hydraulically stable layers.
SM range	National SM range = 5.8-43.9% across the mapped 10-75 cm profile.	Sun et al. (2020): field SWC range = 5.2-51.6% in the Chinese Loess Plateau dataset.	Comparable lower bound, slightly lower upper bound	The Hungarian network spans a broad but somewhat less extreme moisture range, supporting robust cross-texture HG interpretation.
ρ_a range	ρ_a ranged from 94 to 12,441 Ω m, with central-domain values >1,500-2,000 Ω m.	Sun et al. (2020): electrical resistivity range = 13.2-271.9 Ω m.	Much wider and higher range	The higher ρa contrast indicates stronger texture/retention and soil-moisture contrasts in the national Hungarian HG proxy framework.

https://doi.org/10.5194/essd-2026-563
Preprint. Discussion started: 23 September 2026

Texture-state contrast	Sandy soils: SM = 13.9%, ε_r = 7.65, v = 0.119 m ns^{-1}, ρ_a = 1793 Ω m; clayey soils: SM = 27.3%, ε_r = 15.55, v = 0.081 m ns^{-1}, ρ_a = 475 Ω m.	Cao et al. (2020): VSWC was negatively related to sand content and positively related to silt content.	Same direction, stronger multi-parameter expression	This study converts the expected texture-moisture relation into a complete HG state contrast involving dielectric, v and resistivity behavior.
ERT/GPR wetting response	Moisture-rich provinces show higher SM, ε_r, σ and α and lower v and ρa.	Zou et al. (2023): integrated ERT-GPR infiltration experiments used resistivity fitting around a 5% RMSE target.	Same physical direction, broader spatial synthesis	The national maps and 3D model express the same wetting physics at landscape scale rather than only laboratory/event scale.
3D HG representation	Explainable 3D HG state model integrates SM, ε_r, v, σ, α, ρ_a, WHC, WP and HWR across six depths.	Zhou et al. (2001): 3D/time-lapse ERT monitoring of soil water content.	Broader parameter integration and larger scale	The model extends 3D water-content monitoring into a multi-parameter, retention-aware national HG state representation.
Spatial organization	Central moisture-deficient HG province contrasts with higher-moisture eastern, northeastern and northwestern HG provinces.	Peterson et al. (2019) and Hoylman et al. (2019): organized soil-moisture patterns controlled by spatial dynamics, climatic water balance, topography and shallow flow.	Consistent, but extended to HG provinces	The result confirms that HG behavior is spatially organized and adds EM-property structure to soil-moisture pattern theory.

5.2. Texture as the dominant control on water retention and EM proxy

Texture exerted a first-order control on measured SM and the corresponding SM-derived EM proxy ranges, producing stronger contrasts than depth alone. In brief, sandy soils showed lower SM and translated into lower ε_r but higher v and ρ_a proxy values, whereas clayey soils retained more water and translated into higher ε_r, lower v, and lower ρ_a proxy values. This agrees with Cao et al. (2020), who found VSWC to be negatively related to sand content and positively related to silt content, and with Sun et al. (2020), who showed that resistivity-derived soil-water estimates depend strongly on texture, land use, depth and wet/dry conditions. Similarly, Zou et al. (2023) and Abbas et al. (2022) demonstrated that wetting and fine-textured or heterogeneous layers are expressed by decreasing resistivity and increasing ε_r, supporting the paired response observed here. The layered-vadose-zone interpretation is further supported by Tartakovsky et al. (2008), who showed that electrical resistivity data can be used HG to infer subsurface layering, reinforcing the need to treat texture and vertical structure together rather than independently.

The texture dependence also explains why HG behavior cannot be treated as a simple moisture-only signal. Moghadas and Badorreck (2019) showed that the σ–θ relationship is nonlinear and

https://doi.org/10.5194/essd-2026-563
Preprint. Discussion started: 23 September 2026

better captured by machine learning than by a single petrophysical model, while Yosef et al. (2026) emphasized that clay content, soil depth and local soil structure jointly control water-regulation processes. This is consistent with Finkenbiner et al. (2019) and Coppola et al. (2019), who showed that spatial variability in hydraulic properties must be incorporated for reliable water-storage and irrigation modelling. Therefore, texture should be treated as a dominant organizing factor for SM-to-EM calibration, because uniform parameterization would misrepresent retention capacity, expected EM propagation, ρ_a proxy values and hydrological connectivity across the monitoring network.

5.3. Coupling between soil moisture and derived EM proxies

Beyond the texture effect discussed above, the results show a robust petrophysical translation between measured SM and derived EM proxy variables. Across the dataset, higher SM corresponded to higher derived ε_r, σ and α, and to lower derived v and ρ_a, reflecting the equations used to translate pore-water content into expected dielectric, conductive and propagation responses. This multi-parameter coupling is consistent with the review-level conclusion that SM measurements gain hydrological value when they are connected to flow, storage and state-variable interpretation rather than treated as isolated observations (Vereecken et al., 2008). This agrees with Cao et al. (2020), who demonstrated strong dielectric–VSWC relationships across several depth ranges, and with Abbas et al. (2022) and Zou et al. (2023), who showed that increasing water content is expressed by higher ε_r and lower electrical resistivity during vadose-zone wetting and infiltration.

However, this coupling should be interpreted as a physics-informed SM-to-EM proxy translation rather than as independent EM evidence. Sun et al. (2020) showed that resistivity-derived soil-water estimates depend on porosity, saturation, pore-water resistivity, temperature, texture, depth and high- and low-moisture states, while Moghadas and Badorreck (2019) demonstrated that the σ–θ relationship is nonlinear and better represented by machine learning than by a single fixed petrophysical model. Therefore, the observed SM–ε_r–σ–α increase and v–ρ_a decrease support non-invasive soil-water interpretation, but only when texture, retention architecture and site-specific petrophysical assumptions are explicitly considered. This caution is consistent with HG inversion studies showing that GPR-derived hydraulic estimates can be non-unique or stability-limited unless hydrological structure and parameter constraints are included (Jadoon et al., 2008; Busch et al., 2013; Jadoon et al., 2012).

https://doi.org/10.5194/essd-2026-563
Preprint. Discussion started: 23 September 2026

A limitation of the resistivity-related proxy interpretation is that the texture-specific Archie parameters were treated as scenario assumptions rather than calibrated site constants. Because Archie's law is most appropriate for clean, clay-poor porous media, the absolute ρ_a, σ, and α proxy magnitudes, especially for clayey and fine-loam soils, may be affected by clay-mineral surface conduction and by the assigned formation parameters. However, the 30-45 cm buffering zone is not based on Archie-derived resistivity alone; it is also evident in measured SM and in the independently derived dielectric and velocity proxies. Thus, Archie assumptions may affect the magnitude of the resistivity-related response, but are unlikely to fully explain the observed mid-profile pattern. Future field or laboratory geophysical calibration is needed to quantify this sensitivity.

5.4. Hydraulic retention and texture as calibration priors for EM-to-SM estimation

While texture defines the broad proxy contrasts discussed above, HR properties explain why soils with different pore-size distributions store water differently and therefore require different EM-to-SM calibration. WHC showed the strongest and most consistent relationships with ε_r, v and σ, with R^2 values of 0.62–0.79 and ρ mostly between 0.72 and 0.85. The strongest controls occurred at 30–75 cm, especially around 60 cm, where WHC explained ε_r, SM, v and σ most effectively, while WP and HWR became important for strongly retained water and ρ_a. This indicates that the SM-derived EM proxy range is conditioned not only by particle-size class, but by the actual capacity of the soil matrix to store, retain and connect water across the pore network. Coupled inversion studies have similarly demonstrated that geophysical observations can constrain soil hydraulic parameters when hydrological and geophysical models are linked, supporting the use of WHC, WP and HWR as process-level calibration priors rather than simple ancillary variables (Mboh et al., 2012; Jadoon et al., 2012; Busch et al., 2013).

This interpretation is consistent with Achu et al. (2026), who showed that depth-dependent soil attributes, including FC, liquid limit and hydraulic conductivity, substantially improved ML-based prediction and that soil-related attributes explained about 70% of landslide cases. Similarly, Hassan et al. (2024) found that neglecting soil hydraulic-property variability had stronger effects on irrigation and percolation estimates than neglecting vegetation-parameter variability, while Kozma et al. (2024) showed that locally calibrated hydraulic parameters produced the best soil-moisture simulations, with NSME values of 0.50, 0.54 and 0.71 for three Hungarian sites. These comparisons support the significance of our result: retention metrics act as process-level descriptors linking texture and structure to long-term water storage and to the expected ε_r, σ, α and ρa proxy ranges used for future EM-to-SM calibration.

https://doi.org/10.5194/essd-2026-563
Preprint. Discussion started: 23 September 2026

5.5. Integrated proxy indices, spatial calibration provinces and predictive modelling

The integrated proxy indices provided compact descriptors of vertical buffering and expected EM propagation across the monitoring network. EPRI increased from sandy soils to fine-textured groups, while HBI, DA_{10-75}, VD_{10-75} and $\nabla\rho a_{10-75}$ separated moisture-limited and moisture-rich HG domains. The national maps showed low-moisture central domains with lower SM and lower derived ε_r, σ and α but higher derived v and ρa, contrasting with higher-moisture northern, eastern and northwestern regions. The spatial persistence of these provinces is consistent with AGU studies showing that SM variability is organized by recurrent spatial patterns, climatic water balance, topography and shallow subsurface flow rather than by random station-scale noise alone (Peterson et al., 2019; Hoylman et al., 2019; Tyagi et al., 2022; Liu et al., 2022Gupta and Karthikeyan 2024). This spatial organization is consistent with studies showing that spatially distributed soil and hydraulic information is essential for hydrological interpretation. Finkenbiner et al. (2019) showed that HG datasets improved field-capacity estimates by reducing RMSE by 20–25%, AbdelRahman et al. (2022) used IDW-based soil mapping from 460 samples to delineate soil-quality zones, and Coppola et al. (2019) demonstrated the value of spatially distributed agro-hydrological modelling validated with EM-induction-based soil-water storage.

The predictive modelling further shows that retention architecture is a strong basis for defining calibration priors for SM-derived EM proxy ranges. Leakage-safe ML achieved high skill for v (R^2 = 0.75–0.83) and ε_r (R^2 = 0.68–0.81), moderate-to-high skill for σ and α, and depth-dependent improvement for ρ_a, which reached $R^2 \approx 0.86$ at 60–75 cm. This agrees with Moghadas and Badorreck (2019), who showed that ML captured nonlinear σ–θ relationships better than a fixed petrophysical model, and with Pan et al. (2023), who demonstrated that vertical hydraulic heterogeneity in the 0–100 cm root zone can be quantified across large areas using thousands of samples. Therefore, these findings show that the present study extends previous field- and plot-scale HG research by combining vertical proxy indices, national-scale spatial mapping and leakage-safe ML to define calibration provinces from retention-conditioned soil-water behavior. This extension is particularly important because previous AGU studies have demonstrated strong field-scale monitoring and inversion capacity, but generally did not integrate multi-depth national mapping, retention metrics and explainable 3D HG state synthesis in a single framework (Zhou et al., 2001; Jadoon et al., 2008; Steelman et al., 2012; Busch et al., 2013; Cheng et al., 2023). This integrated interpretation is summarized in Fig. 12, which links prior process-level HG evidence (Fig. 12A), the observed HG state transition (Fig.

https://doi.org/10.5194/essd-2026-563
Preprint. Discussion started: 23 September 2026

12B), the 30-45 cm buffering zone (Fig. 12C), and the explainable 3D HG province model (Fig. 12D) into a single national-scale HG framework.

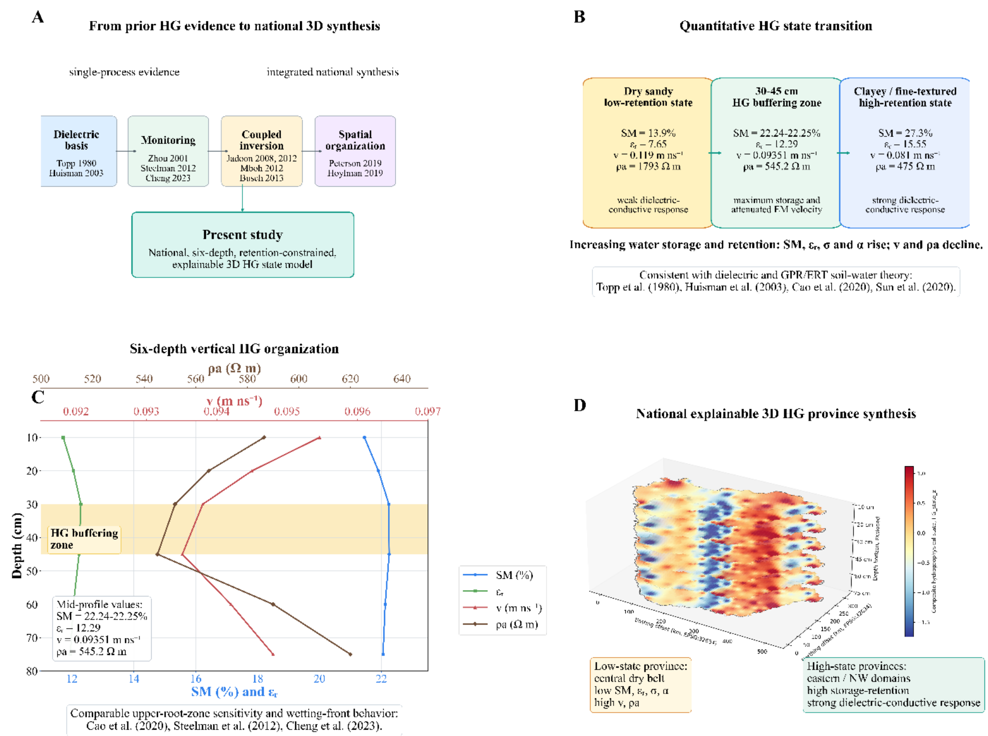

Fig. 12. Discussion synthesis linking prior HG evidence with the present national-scale explainable 3D SM-to-EM proxy framework. (A) Progression from dielectric, monitoring, coupled-inversion, and spatial HG studies toward the integrated six-depth framework developed here. (B) Quantitative transition from low-moisture, sandy, low-retention states to the 30-45 cm proxy buffering zone and high-retention fine-textured states. (C) Vertical organization of SM, ε_r, v, and ρ_a, highlighting the mid-profile buffering zone where measured water storage increases and derived v decreases. (D) Explainable 3D proxy province model showing vertically persistent low-state and high-state domains across Hungary.

6. Conclusion

This study developed a national six-depth SM-to-EM proxy database showing how measured soil moisture, texture, and hydraulic-retention architecture translate into expected electromagnetic proxy ranges across the vadose-zone profile. By deriving and integrating EM proxy variables across six depths, the analysis identified a consistent mid-profile buffering zone at 30–45 cm, where measured water storage increased and the translated proxy response showed higher ε_r, σ, and α with lower v and ρ_a. This depth interval therefore represents a key transition zone where atmospheric forcing is dampened and subsurface hydraulic structure shapes the expected EM response used for future calibration.

The results show that texture provides the first-order spatial and vertical contrast in measured SM and derived EM proxy ranges, while HR variables, particularly water-holding capacity, wilting point, and strongly bound water fractions, provide additional calibration-relevant information. Retention- and texture-based predictors achieved high model skill for SM-derived ε_r and v proxy values, indicating that future EM-to-SM estimation should be constrained by pore-water storage, retention capacity, and hydraulic connectivity.

The explainable 3D proxy state model further strengthens this interpretation by synthesizing measured SM, hydraulic variables, and derived EM proxy variables into a depth-resolved composite representation of the root-zone system. The model revealed vertically persistent proxy provinces across Hungary, distinguishing higher-moisture and more retentive domains from lower-moisture and more resistive domains with faster expected EM propagation. This provides a process-based spatial framework linking local station-scale SM measurements to a national calibration layer for future GPR, resistivity, and EM-based soil-moisture estimation.

Overall, this study provides a scalable calibration basis for interpreting soil-water dynamics through texture- and retention-conditioned SM-to-EM proxy translation. Beyond the national soil-moisture analysis, the approach has decision-support value for vadose-zone monitoring, drone GPR survey design, resistivity-based SM estimation, agricultural water management, drought assessment, groundwater-recharge evaluation, and future non-invasive soil-moisture mapping. Its transferability should be tested through independent GPR, resistivity, and EM validation, sensitivity analysis of petrophysical assumptions, and time-lapse 3D modelling across contrasting soil and climate settings.

References

1. Abbas, M., Deparis, J., Isch, A., Mallet, C., Jodry, C., Azaroual, M., Abbar, B., & Baltassat, J. M. (2022). Hydrogeophysical characterization and determination of petrophysical parameters by integrating geophysical and hydrogeological data at the limestone vadose zone of the Beauce aquifer. Journal of Hydrology, 615, Article 128725. https://doi.org/10.1016/j.jhydrol.2022.128725

https://doi.org/10.5194/essd-2026-563
Preprint. Discussion started: 23 September 2026

2. AbdelRahman, M. A. E., Farg, E., Saleh, A. M., Sayed, M., Abutaleb, K., Arafat, S. M., & Elsharkawy, M. M. (2022). Mapping of soils and land-related environmental attributes in modern agriculture systems using geomatics. Sustainable Water Resources Management, 8(4), Article 116. https://doi.org/10.1007/s40899-022-00704-2
3. Abdelsamei, Enas, Tímár, Attila, Sheishah, Diaa, Blanka-Végi, Viktória, Hegyi, Alexandru, Runa, Boglárka, Balogh, Olivér, Ali, Ahmed M. and Sipos, György. "Detection of seepage zones in artificial levees: A case study at the Körös River, Hungary" *Open Geosciences*, vol. 16, no. 1, 2024, pp. 20220744. https://doi.org/10.1515/geo-2022-0744
4. Achu, A. L., Aju, C. D., Thomas, J., & Gopinath, G. (2026). Catena matters: Enhancing landslide prediction with soil profile characteristics and explainable AI. Engineering Geology, 364, Article 108599. https://doi.org/10.1016/j.enggeo.2026.108599
5. Archie, G. E. (1942). The electrical resistivity log as an aid in determining some reservoir characteristics. Transactions of the AIME, 146(1), 54-62. https://doi.org/10.2118/942054-G
6. Bo, Y., Li, X., Liu, K., Wang, S., Tang, Q., Jiang, Y., Li, Z., Lu, S., Wang, L., Feng, C., Zhou, Z., & Zhou, G. (2026). Quantifying historical and future surface soil moisture drying using deep learning and remote sensing. *Earth's Future, 14*(3), e2025EF006261. https://doi.org/10.1029/2025EF006261
7. Breiman, L. (2001). Random forests. Machine Learning, 45, 5-32. https://doi.org/10.1023/A:1010933404324
8. Busch, S., Weihermuller, L., Huisman, J. A., Steelman, C. M., Endres, A. L., Vereecken, H., & van der Kruk, J. (2013). Coupled hydrogeophysical inversion of time-lapse surface GPR data to estimate hydraulic properties of a layered subsurface. Water Resources Research, 49(12), 8480-8494. https://doi.org/10.1002/2013WR013992
9. Cao, Q., Song, X., Wu, H., Gao, L., Liu, F., Yang, S., & Zhang, G. (2020). Mapping the response of volumetric soil water content to an intense rainfall event at the field scale using GPR. Journal of Hydrology, 583, Article 124605. https://doi.org/10.1016/j.jhydrol.2020.124605
10. Cheng, Q., Su, Q., Binley, A., Liu, J., Zhang, Z., & Chen, X. (2023). Estimation of surface soil moisture by a multi-elevation UAV-based ground penetrating radar. Water Resources Research, 59(2), Article e2022WR032621. https://doi.org/10.1029/2022WR032621

11. Coppola, A., Dragonetti, G., Sengouga, A., Lamaddalena, N., Comegna, A., Basile, A., Noviello, N., & Nardella, L. (2019). Identifying optimal irrigation water needs at district scale by using a physically based agro-hydrological model. Water, 11(4), Article 841. https://doi.org/10.3390/w11040841
12. Fiala, K., et al. (2018a). Operational drought and water scarcity monitoring system in Hungary. Hidrologiai Kozlony, 98(3), 3-12. https://publicatio.bibl.u-szeged.hu/17598/
13. Fiala, K., Barta, K., Benyhe, B., et al. (2018b). Development of an operational drought and water scarcity monitoring system in Hungary. Global Water Partnership. https://www.gwp.org/globalassets/global/gwp-cee_files/idmp-cee/idmp-drought-monitoring-hungary.pdf
14. Finkenbiner, C. E., Franz, T. E., Gibson, J., Heeren, D. M., Luck, J., & Rudnick, D. R. (2019). Integration of hydrogeophysical datasets and empirical orthogonal functions for improved irrigation water management. Precision Agriculture, 20, 78-100. https://doi.org/10.1007/s11119-018-9582-5
15. Friedman, J. H. (2001). Greedy function approximation: A gradient boosting machine. The Annals of Statistics, 29(5), 1189-1232. https://doi.org/10.1214/aos/1013203451
16. Geurts, P., Ernst, D., & Wehenkel, L. (2006). Extremely randomized trees. Machine Learning, 63, 3-42. https://doi.org/10.1007/s10994-006-6226-1
17. Gupta, A., & Karthikeyan, L. (2024). Role of initial conditions and meteorological drought in soil moisture drought propagation: An event-based causal analysis over South Asia. *Earth's Future, 12*(10), e2024EF004674. https://doi.org/10.1029/2024EF004674
18. Grayson, R. B., Western, A. W., & Bloschl, G. (1997). Preferred states in spatial soil moisture patterns: Local and nonlocal controls. Water Resources Research, 33(12), 2897-2908. https://doi.org/10.1029/97WR02174
19. Hassan, S. B. M., Dragonetti, G., Comegna, A., Lamaddalena, N., & Coppola, A. (2024). Analyzing the role of soil and vegetation spatial variability in modelling hydrological processes for irrigation optimization at large scale. Irrigation Science, 42, 249-267. https://doi.org/10.1007/s00271-023-00882-7
20. Hayley, K., Bentley, L. R., & Gharibi, M. (2009). Time-lapse electrical resistivity monitoring of salt-affected soil and groundwater. Water Resources Research, 45(7), Article 2008WR007616. https://doi.org/10.1029/2008WR007616
21. Hoylman, Z. H., Jencso, K. G., Hu, J., Holden, Z. A., Martin, J. T., & Gardner, W. P. (2019). The climatic water balance and topography control spatial patterns of

atmospheric demand, soil moisture, and shallow subsurface flow. Water Resources Research, 55(3), 2370-2389. https://doi.org/10.1029/2018WR023302

22. Hsu, H., & Dirmeyer, P. A. (2023). Uncertainty in projected critical soil moisture values in CMIP6 affects the interpretation of a more moisture-limited world. *Earth's Future, 11*(6), e2023EF003511. https://doi.org/10.1029/2023EF003511
23. Huisman, J. A., Hubbard, S. S., Redman, J. D., & Annan, A. P. (2003). Measuring soil water content with ground penetrating radar: A review. Vadose Zone Journal, 2(4), 476-491. https://doi.org/10.2136/vzj2003.4760
24. Jadoon, K. Z., Slob, E., Vanclooster, M., Vereecken, H., & Lambot, S. (2008). Uniqueness and stability analysis of hydrogeophysical inversion for time-lapse ground-penetrating radar estimates of shallow soil hydraulic properties. Water Resources Research, 44(9), Article 2007WR006639. https://doi.org/10.1029/2007WR006639
25. Jadoon, K. Z., Weihermuller, L., Scharnagl, B., Kowalsky, M. B., Bechtold, M., Hubbard, S. S., Vereecken, H., & Lambot, S. (2012). Estimation of soil hydraulic parameters in the field by integrated hydrogeophysical inversion of time-lapse ground-penetrating radar data. Vadose Zone Journal, 11(4), Article vzj2011.0177. https://doi.org/10.2136/vzj2011.0177
26. Kozma, Z., Decsi, B., Acs, T., Jolankai, Z., Manninger, M., Moricz, N., Illes, G., Barna, G., Mako, A., & Szabo, B. (2024). Functional evaluation of different soil hydraulic parametrizations in hydrological simulations reveals different model efficiency for soil moisture and water budget. Journal of Hydrology and Hydromechanics, 72(3), 312-335. https://doi.org/10.2478/johh-2024-0013
27. Liu, X., Liu, W., Tang, Q., Liu, B., Wada, Y., & Yang, H. (2022). Global agricultural water scarcity assessment incorporating blue and green water availability under future climate change. *Earth's Future, 10*(4), e2021EF002567. https://doi.org/10.1029/2021EF002567
28. Mboh, C. M., Huisman, J. A., Zimmermann, E., & Vereecken, H. (2012). Coupled hydrogeophysical inversion of streaming potential signals for unsaturated soil hydraulic properties. Vadose Zone Journal, 11(2), Article vzj2011.0115. https://doi.org/10.2136/vzj2011.0115
29. Moghadas, D., & Badorreck, A. (2019). Machine learning to estimate soil moisture from geophysical measurements of electrical conductivity. Near Surface Geophysics, 17(2), 181-195. https://doi.org/10.1002/nsg.12036

https://doi.org/10.5194/essd-2026-563
Preprint. Discussion started: 23 September 2026

30. Natural Resources Conservation Service. (n.d.). *Soil texture calculator*. United States Department of Agriculture. https://www.nrcs.usda.gov/resources/education-and-teaching-materials/soil-texture-calculator Accessed May 04, 2026.
31. Operational Drought and Water Scarcity Monitoring System (DWMS). (n.d.). Aszaly monitoring rendszer: Station data and system description. DWMS.
32. OVF. (2024). Protection against drought. https://www.ovf.hu/en/flood-protection-water-damage-control/protection-against-drought
33. Pan, H., Ran, Q., Hong, Y., Wang, J., Chen, X., & Ye, S. (2023). Long-term impacts of ecosystem restoration on saturated hydraulic conductivity in the Loess Plateau. Journal of Hydrology, 620, Article 129337. https://doi.org/10.1016/j.jhydrol.2023.129337
34. Patil, N. G., & Rajput, G. S. (2009). Evaluation of water retention functions and computer program "Rosetta" in predicting soil water characteristics of seasonally impounded shrink-swell soils. Journal of Irrigation and Drainage Engineering, 135(3), 286-294. https://doi.org/10.1061/(ASCE)IR.1943-4774.0000007
35. Pearson, K. (1895). Note on regression and inheritance in the case of two parents. Proceedings of the Royal Society of London, 58, 240-242. https://doi.org/10.1098/rspl.1895.0041
36. Peterson, A. M., Helgason, W. H., & Ireson, A. M. (2019). How spatial patterns of soil moisture dynamics can explain field-scale soil moisture variability: Observations from a sodic landscape. Water Resources Research, 55(5), 4410-4426. https://doi.org/10.1029/2018WR023329
37. Sheishah, D., Kiss, T., Borza, T., Fiala, K., Kozak, P., Abdelsamei, E., Toth, C., Grenerczy, G., Pall, D. G., & Sipos, G. (2023a). Mapping subsurface defects and surface deformation along the artificial levee of the Lower Tisza River, Hungary. Natural Hazards, 117(2), 1647-1671. https://doi.org/10.1007/s11069-023-05922-1
38. Sheishah, D., Sipos, G., Barta, K., Abdelsamei, E., Hegyi, A., Onaca, A., & Abbas, A. M. (2023b). Comparative evaluation of the material of the artificial levees. Journal of Environmental Geography, 16(1-4), 1-10. https://doi.org/10.14232/jengeo-2023-44452
39. Sheishah, D., Abdelsamei, E., Abbas, A. M., Blanka-Vegi, V., Barta, K., Aldeep, M., Ali, A. M., & Sipos, G. (2026a). Applying different features of GPR hyperbolic reflections to refine cavity identification in a complex environment. Modeling Earth Systems and Environment, 12, Article 22. https://doi.org/10.1007/s40808-025-02676-6
40. Sheishah, D., Abdelsamei, E., Blanka-Vegi, V., Filyo, D., Magyar, G., Mohsen, A., Hegyi, A., Abbas, A. M., Toth, C., Borza, T., Kozak, P., Onaca, A., Hajdu, S., & Sipos,

https://doi.org/10.5194/essd-2026-563
Preprint. Discussion started: 23 September 2026

G. (2026b). Mapping complex artificial levees and predicting their condition using machine learning-integrated electrical resistivity tomography. Water, 18(7), Article 826. https://doi.org/10.3390/w18070826

41. Sheishah, D., Abdelsamei, E., Blanka-Végi, V., Barta, K., Ali, A. M., Abualhin, K., Al-Halbouni, D., Dorigo, W., and Sipos, G.: A National Depth-Resolved Soil-Moisture-to-Electromagnetic Proxy Database for Hydrogeophysical Monitoring [data set], Zenodo, https://doi.org/10.5281/zenodo.21370490, 2026c.
42. Shepard, D. (1968). A two-dimensional interpolation function for irregularly-spaced data. In Proceedings of the 1968 23rd ACM National Conference (pp. 517-524). Association for Computing Machinery. https://doi.org/10.1145/800186.810616
43. Spearman, C. (2010). The proof and measurement of association between two things. International Journal of Epidemiology, 39(5), 1137-1150. https://doi.org/10.1093/ije/dyq191
44. Steelman, C. M., Endres, A. L., & Jones, J. P. (2012). High-resolution ground-penetrating radar monitoring of soil moisture dynamics: Field results, interpretation, and comparison with unsaturated flow model. Water Resources Research, 48(9), Article 2011WR011414. https://doi.org/10.1029/2011WR011414
45. Sun, H., Wang, Y., Zhao, Y., Zhang, P., Song, Y., He, M., Zhang, C., Tong, Y., Zhou, J., Qi, L., & Xu, L. (2020). Assessing the value of electrical resistivity derived soil water content: Insights from a case study in the Critical Zone of the Chinese Loess Plateau. Journal of Hydrology, 589, Article 125132. https://doi.org/10.1016/j.jhydrol.2020.125132
46. Tartakovsky, A. M., Bolster, D., & Tartakovsky, D. M. (2008). Hydrogeophysical approach for identification of layered structures of the vadose zone from electrical resistivity data. Vadose Zone Journal, 7(4), 1253-1260. https://doi.org/10.2136/vzj2008.0009
47. Topp, G. C., Davis, J. L., & Annan, A. P. (1980). Electromagnetic determination of soil water content: Measurements in coaxial transmission lines. Water Resources Research, 16(3), 574-582. https://doi.org/10.1029/WR016i003p00574
48. Tyagi, S., Zhang, X., Saraswat, D., Sahany, S., Mishra, S. K., & Niyogi, D. (2022). Flash drought: Review of concept, prediction and the potential for machine learning, deep learning methods. *Earth's Future, 10*(11), e2022EF002723. https://doi.org/10.1029/2022EF002723

https://doi.org/10.5194/essd-2026-563
Preprint. Discussion started: 23 September 2026

49. Vereecken, H., Huisman, J. A., Bogena, H., Vanderborght, J., Vrugt, J. A., & Hopmans, J. W. (2008). On the value of soil moisture measurements in vadose zone hydrology: A review. Water Resources Research, 44(4), Article 2008WR006829. https://doi.org/10.1029/2008WR006829
50. Yosef, B. A., Basile, A., Coppola, A., Ungaro, F., Zucca, C., & Bancheri, M. (2026). Soil indicators for ecosystem services: A focus on water regulation. SOIL, 12(1), 347-369. https://doi.org/10.5194/soil-12-347-2026
51. Yu, Y., Huisman, J. A., Klotzsche, A., Vereecken, H., & Weihermuller, L. (2022). Coupled full-waveform inversion of horizontal borehole ground penetrating radar data to estimate soil hydraulic parameters: A synthetic study. Journal of Hydrology, 610, Article 127817. https://doi.org/10.1016/j.jhydrol.2022.127817
52. Yu, Y., Huisman, J. A., Klotzsche, A., Tao, X., & Zhang, K. (2026). Coupled Bayesian inversion of time-lapse dispersive ground penetrating radar data to estimate soil hydraulic parameters. Journal of Hydrology, 674, Article 135435. https://doi.org/10.1016/j.jhydrol.2026.135435
53. Zhou, Q. Y., Shimada, J., & Sato, A. (2001). Three-dimensional spatial and temporal monitoring of soil water content using electrical resistivity tomography. Water Resources Research, 37(2), 273-285. https://doi.org/10.1029/2000WR900284
54. Zhou, J., Teuling, A. J., Seneviratne, S. I., & Hirsch, A. L. (2024). Soil moisture-temperature coupling increases population exposure to future heatwaves. *Earth's Future, 12*(7), e2024EF004697. https://doi.org/10.1029/2024EF004697
55. Zou, C., Zhang, S., Jiang, X., & Chen, F. (2023). Monitoring and characterization of water infiltration in soil unsaturated zone through an integrated geophysical approach. CATENA, 230, Article 107243. https://doi.org/10.1016/j.catena.2023.107243

Data Availability

The soil-moisture data used in this study were obtained from the Operational Drought and Water Scarcity Monitoring System (DWMS) available at https://vizhiany.vizugy.hu/. All derived hydrogeophysical variables, figures, tables, interpolation products, and 3D model outputs were generated using reproducible Python workflows developed for this manuscript. The main analysis pipeline, *SM_geophysics_full_pipeline_v8.py*, performs data harmonization, hydrogeophysical parameter calculation, statistical analysis, machine-learning evaluation, mapping, and manuscript-ready figure/table export. The national 3D visualization was

https://doi.org/10.5194/essd-2026-563
Preprint. Discussion started: 23 September 2026

produced using *build_explainable_3d_hg_model.py*, which integrates SM, ε_r, ν, σ, ρa, α, and HR metrics across the six soil depths into an explainable hydrogeophysical state model. Additional 3D and composite model products were generated with *build_3d_hydrogeophysical_model.py* and *build_hg_model_figure_suite.py*. These scripts, together with the processed tables, high-resolution figures, and interactive 3D HTML model, will be publicly available from Zenodo (Sheishah et al., 2026c) at https://doi.org/10.5281/zenodo.21370490 upon publication.

Conflict of Interest

The authors declare no conflict of interest.

Funding

The publication was financially supported by the University of Szeged Open Access Fund, Grant ID: 8918.

Author contributions

DS: conceptualization, methodology, software, formal analysis, data curation, visualization, writing original draft. EA: data curation, investigation, validation, writing review and editing. VBV: investigation, methodology, writing review and editing. KB: supervision, investigation, writing review and editing. AMA: validation, geophysical interpretation, writing review and editing. KA: visualization, Earth-system data interpretation, writing review and editing. DAH: conceptualization, writing review and editing. WD: soil-moisture data expertise, validation, writing review and editing. GS: conceptualization, supervision, project coordination, writing review and editing. All authors approved the final manuscript.

Appendix A

https://doi.org/10.5194/essd-2026-563
Preprint. Discussion started: 23 September 2026

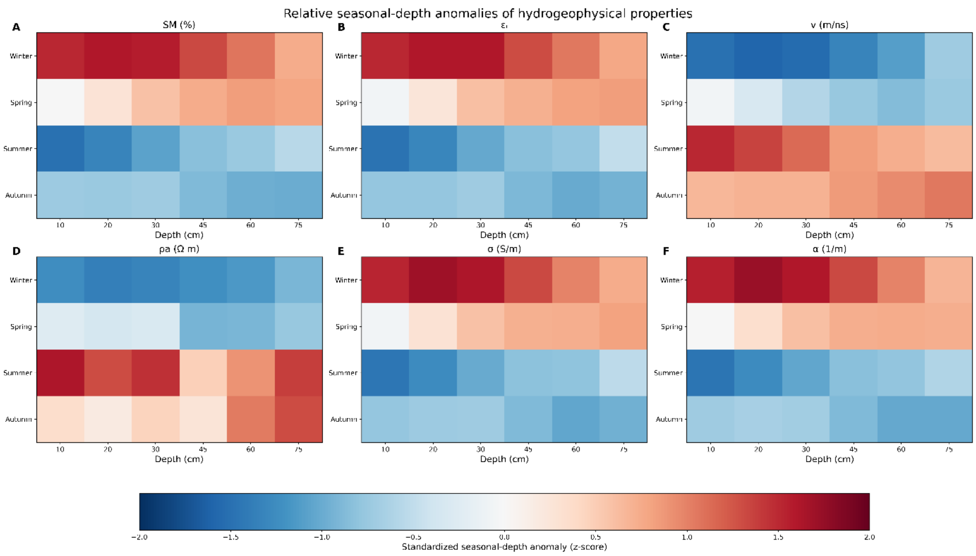

Fig. A1. Relative seasonal–depth anomalies of (A) SM, (B) ε_r, (C) v, (D) ρa, (E) σ, and (F) α expressed as standardized z-scores. Positive anomalies (red) indicate values above the overall annual–depth mean, whereas negative anomalies (blue) indicate values below the mean. Winter and spring are characterized by positive SM, ε_r, σ, and α anomalies and negative v and ρa anomalies, while summer exhibits the opposite pattern. The anomaly structure reveals coherent seasonal controls on HG behavior throughout the 10–75 cm soil profile.

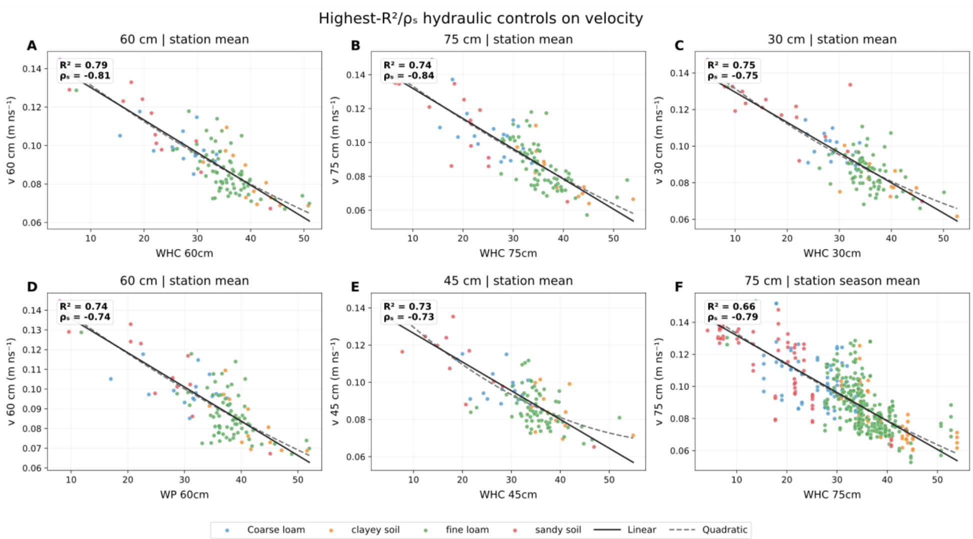

https://doi.org/10.5194/essd-2026-563
Preprint. Discussion started: 23 September 2026

Fig. A2. Strongest HR controls on v. Panels A-F show the highest R^2/ρ_s relationships between retention variables, mainly WHC and WP, and v at selected depths and aggregation scales. v decreases systematically with increasing retention capacity, indicating that higher-moisture, more retentive soils exhibit higher ε_r and slower EM wave propagation. Points are colored by texture class; solid and dashed lines represent linear and quadratic fits, respectively.

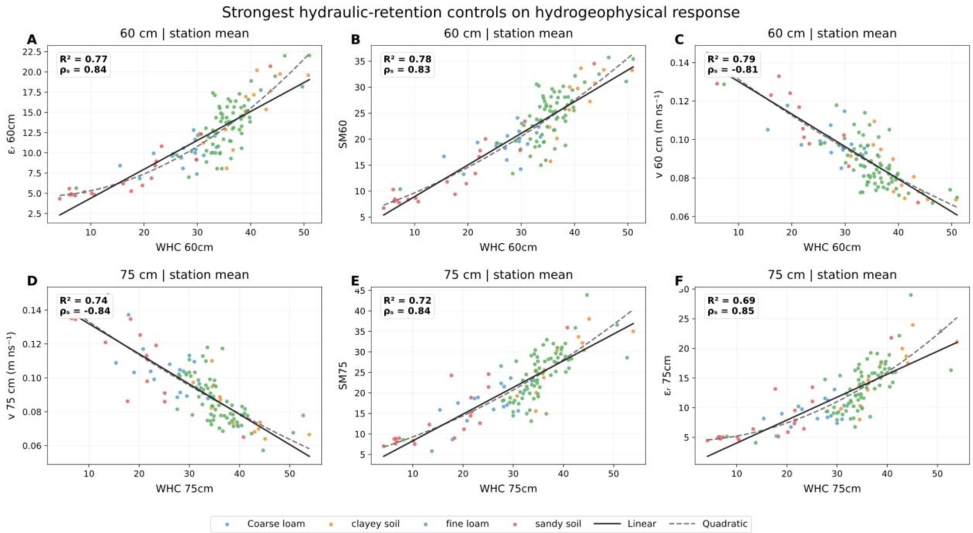

Fig. A3. Strongest HR controls on the integrated HG response. Panels A-F show the highest R^2/ρ_s relationships linking WHC to ε_r, SM, and v at 60 and 75 cm. Higher WHC is associated with increased SM and ε_r but reduced v, confirming that hydraulic retention governs both water storage and EM propagation. Points are colored by texture class; solid and dashed lines represent linear and quadratic fits, respectively.

https://doi.org/10.5194/essd-2026-563
Preprint. Discussion started: 23 September 2026

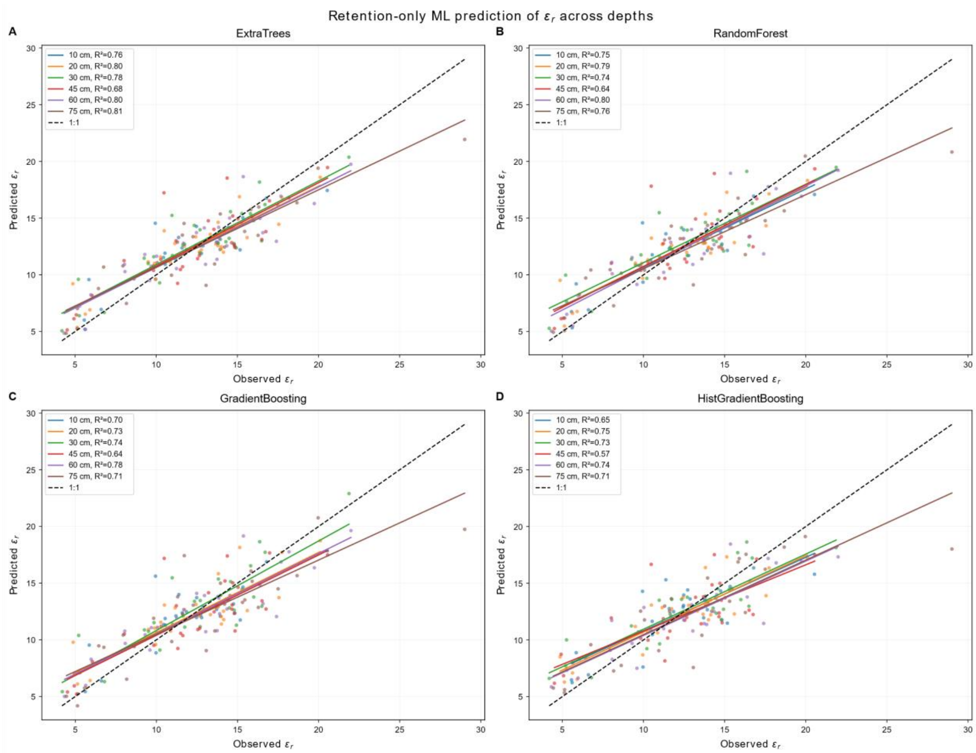

Fig. A4 Retention-only machine-learning prediction of ε_r across depths. Observed versus predicted ε_r values for four machine-learning algorithms (ExtraTrees, Random Forest, Gradient Boosting, and HistGradientBoosting) at six depths (10–75 cm). Dashed lines indicate the 1:1 relationship. Predictive skill increased with depth, with the highest performance achieved at 60–75 cm (R^2 up to 0.81), demonstrating strong HR control on dielectric behavior.

https://doi.org/10.5194/essd-2026-563
Preprint. Discussion started: 23 September 2026

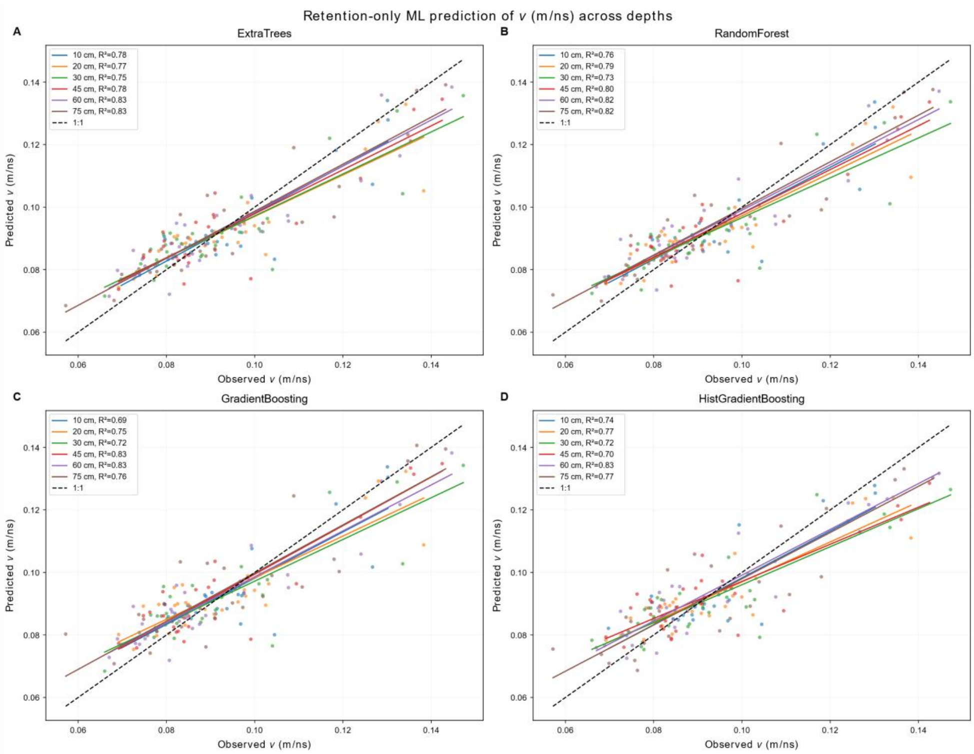

Fig. A5 Retention-only machine-learning prediction of v across depths. Observed versus predicted v values for four machine-learning algorithms at six depths (10–75 cm). Dashed lines indicate the 1:1 relationship. v exhibited consistently high predictive performance (R^2 = 0.75–0.83), confirming that soil HR properties exert stable control on EM wave propagation throughout the profile.

https://doi.org/10.5194/essd-2026-563
Preprint. Discussion started: 23 September 2026

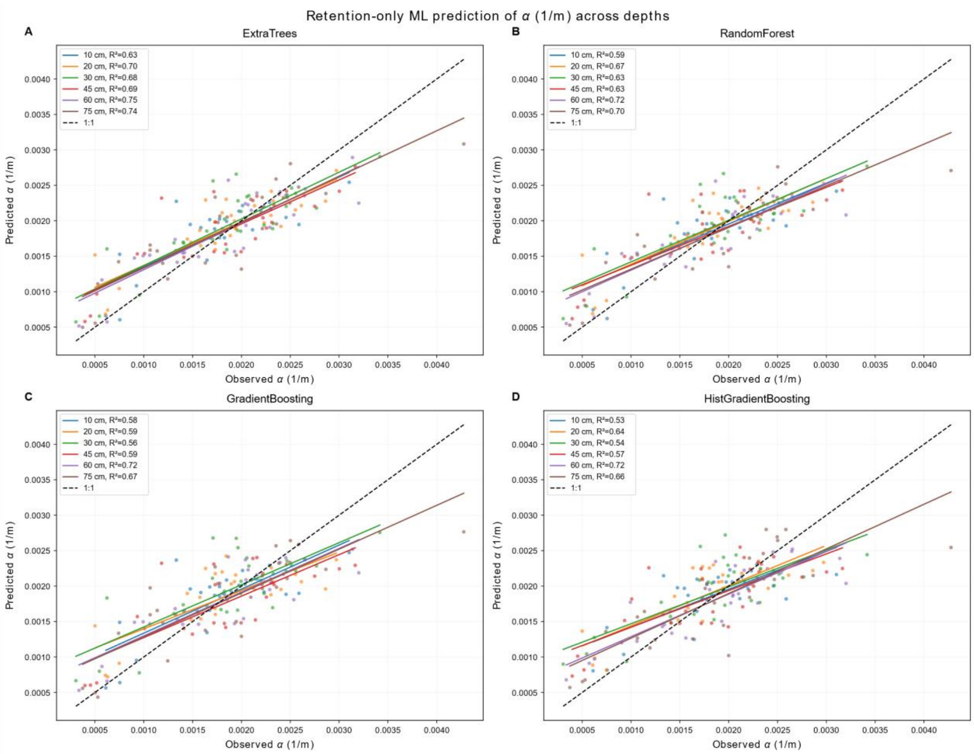

Fig. A6 Retention-only machine-learning prediction of α across depths. Observed versus predicted α values for four machine-learning algorithms at six depths (10–75 cm). Dashed lines indicate the 1:1 relationship. Prediction performance improved with depth ($R^2 \approx 0.63$–0.75), indicating that α increasingly reflects intrinsic HR characteristics in deeper soil horizons.

https://doi.org/10.5194/essd-2026-563
Preprint. Discussion started: 23 September 2026

Open Access Earth System Science Data Discussions

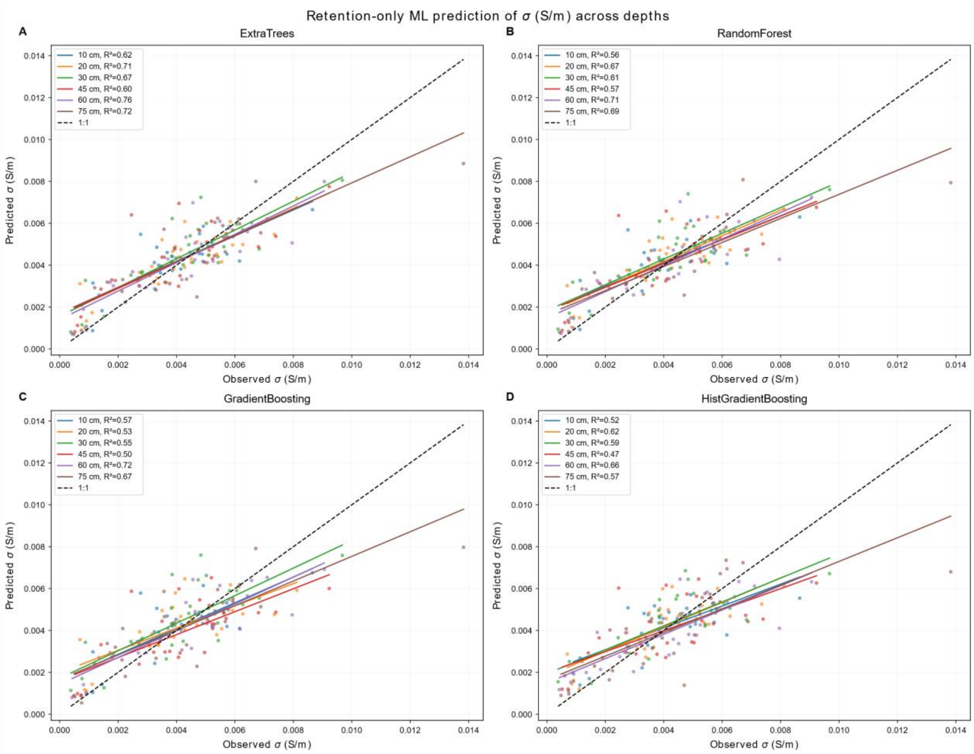

Fig. A7 Retention-only machine-learning prediction of σ across depths. Observed versus predicted σ values for four machine-learning algorithms at six depths (10–75 cm). Dashed lines indicate the 1:1 relationship. Conductivity was predicted with moderate-to-high accuracy ($R^2 \approx 0.62$–0.76), with the strongest performance observed at 60–75 cm, reflecting increasing hydraulic control on conductive pathways with depth.

Table A1. Full ranked matrix of HR controls on HG properties. Relationships are reported for station means and station-season means using r, ρ, linear R^2, quadratic R^2, and best R^2 from the tested fits. Variables are ranked by combined strength; the condensed main-text Table 1 reports only the strongest representative relationships.

Depth (cm)	HR predictor	HG response	r	ρ	Linear R²	Quadratic R²	Best R²	Combined strength
60	WHC 60cm	ε_r 60cm	0.85	0.84	0.72	0.77	0.77	0.81
60	WHC 60cm	SM60	0.88	0.83	0.77	0.78	0.78	0.81
60	WHC 60cm	v 60 cm (m ns^{-1})	- 0.89	- 0.81	0.79	0.79	0.79	0.80
75	WHC 75cm	v 75 cm (m ns^{-1})	- 0.86	- 0.84	0.74	0.74	0.74	0.79
75	WHC 75cm	SM75	0.84	0.84	0.70	0.72	0.72	0.78
75	WHC 75cm	ε_r 75cm	0.80	0.85	0.65	0.69	0.69	0.77

https://doi.org/10.5194/essd-2026-563
Preprint. Discussion started: 23 September 2026

30	WHC 30cm	SM30	0.85	0.77	0.72	0.73	0.73	0.75
30	WHC 30cm	v 30 cm (m ns^{-1})	- 0.86	- 0.75	0.74	0.75	0.75	0.75
30	WHC 30cm	ε_r 30cm	0.82	0.79	0.68	0.71	0.71	0.75
60	WP 60cm	v 60 cm (m ns^{-1})	- 0.86	- 0.74	0.74	0.74	0.74	0.74
60	WP 60cm	SM60	0.84	0.76	0.70	0.72	0.72	0.74
45	WHC 45cm	SM45	0.84	0.77	0.70	0.70	0.70	0.74
60	WP 60cm	ε_r 60cm	0.81	0.77	0.65	0.70	0.70	0.73
45	WHC 45cm	ε_r 45cm	0.82	0.78	0.67	0.68	0.68	0.73
45	WHC 45cm	v 45 cm (m ns^{-1})	- 0.85	- 0.73	0.71	0.73	0.73	0.73
75	WHC 75cm	v 75 cm (m ns^{-1})	- 0.81	- 0.79	0.66	0.66	0.66	0.72
75	WHC 75cm	SM75	0.79	0.80	0.63	0.64	0.64	0.72
75	WP 75cm	v 75 cm (m ns^{-1})	- 0.82	- 0.75	0.68	0.68	0.68	0.72
75	WHC 75cm	ε_r 75cm	0.76	0.80	0.57	0.61	0.61	0.70
60	WHC 60cm	sigma 60 cm (S m^{-1})	0.77	0.77	0.60	0.63	0.63	0.70
30	WP 30cm	v 30 cm (m ns^{-1})	- 0.84	- 0.70	0.70	0.70	0.70	0.70
60	WHC 60cm	v 60 cm (m ns^{-1})	- 0.81	- 0.74	0.66	0.66	0.66	0.70
60	HWR 60cm pF6.2	ε_r 60cm	0.78	0.77	0.61	0.62	0.62	0.70
60	WHC 60cm	SM60	0.80	0.75	0.64	0.64	0.64	0.70
30	WP 30cm	SM30	0.82	0.72	0.67	0.67	0.67	0.70
30	HWR 30cm pF4.2	v 30 cm (m ns^{-1})	- 0.74	- 0.71	0.55	0.68	0.68	0.70
45	HWR 45cm pF4.2	SM45	0.78	0.73	0.61	0.66	0.66	0.70
45	HWR 45cm pF4.2	ε_r 45cm	0.80	0.74	0.63	0.65	0.65	0.69
75	WP 75cm	SM75	0.79	0.76	0.63	0.63	0.63	0.69
30	HWR 30cm pF4.2	SM30	0.78	0.72	0.60	0.66	0.66	0.69
60	WHC 60cm	ε_r 60cm	0.77	0.76	0.59	0.62	0.62	0.69
30	WP 30cm	ε_r 30cm	0.78	0.73	0.61	0.65	0.65	0.69
60	HWR 60cm pF4.2	SM60	0.79	0.74	0.62	0.64	0.64	0.69
60	HWR 60cm pF4.2	ε_r 60cm	0.79	0.75	0.62	0.63	0.63	0.69
60	HWR 60cm pF4.2	v 60 cm (m ns^{-1})	- 0.76	- 0.73	0.57	0.64	0.64	0.69
20	WHC 20cm	SM20	0.81	0.72	0.65	0.65	0.65	0.69
20	WHC 20cm	v 20 cm (m ns^{-1})	- 0.81	- 0.69	0.65	0.68	0.68	0.68
45	HWR 45cm pF6.2	ε_r 45cm	0.76	0.75	0.58	0.62	0.62	0.68
30	HWR 30cm pF4.2	ε_r 30cm	0.78	0.73	0.61	0.63	0.63	0.68
20	WHC 20cm	ε_r 20cm	0.79	0.74	0.63	0.63	0.63	0.68
45	HWR 45cm pF4.2	v 45 cm (m ns^{-1})	- 0.74	- 0.69	0.54	0.67	0.67	0.68
75	WP 75cm	ε_r 75cm	0.75	0.77	0.56	0.59	0.59	0.68
10	HWR 10cm pF4.2	SM10	0.70	0.71	0.49	0.64	0.64	0.68
60	HWR 60cm pF6.2	SM60	0.75	0.76	0.56	0.60	0.60	0.68
30	WHC 30cm	sigma 30 cm (S m^{-1})	0.77	0.74	0.59	0.61	0.61	0.68

https://doi.org/10.5194/essd-2026-563
Preprint. Discussion started: 23 September 2026

10	WHC 10cm	SM10	0.80	0.71	0.64	0.65	0.65	0.68
10	WHC 10cm	v 10 cm (m ns^{-1})	- 0.80	- 0.68	0.64	0.68	0.68	0.68
10	HWR 10cm pF4.2	v 10 cm (m ns^{-1})	- 0.67	- 0.70	0.45	0.65	0.65	0.67
10	HWR 10cm pF4.2	ε_r 10cm	0.71	0.72	0.50	0.62	0.62	0.67
10	WHC 10cm	ε_r 10cm	0.79	0.72	0.62	0.62	0.62	0.67
75	HWR 75cm pF6.2	ε_r 75cm	0.78	0.73	0.60	0.60	0.60	0.67
45	HWR 45cm pF6.2	SM45	0.73	0.74	0.53	0.59	0.59	0.67
45	WP 45cm	SM45	0.80	0.68	0.65	0.65	0.65	0.66
45	WP 45cm	v 45 cm (m ns^{-1})	- 0.82	- 0.64	0.67	0.69	0.69	0.66
20	HWR 20cm pF4.2	v 20 cm (m ns^{-1})	- 0.74	- 0.70	0.55	0.62	0.62	0.66
75	WP 75cm	v 75 cm (m ns^{-1})	- 0.78	- 0.71	0.60	0.61	0.61	0.66
45	WP 45cm	ε_r 45cm	0.78	0.70	0.61	0.61	0.61	0.66
75	HWR 75cm pF4.2	SM75	0.72	0.73	0.52	0.58	0.58	0.65
75	HWR 75cm pF4.2	v 75 cm (m ns^{-1})	- 0.69	- 0.72	0.48	0.59	0.59	0.65
60	WHC 60cm	alpha 60 cm (m^{-1})	0.77	0.72	0.59	0.59	0.59	0.65
75	WHC 75cm	sigma 75 cm (S m^{-1})	0.71	0.77	0.51	0.53	0.53	0.65
20	HWR 20cm pF4.2	SM20	0.76	0.70	0.58	0.60	0.60	0.65
20	WP 20cm	ε_r 20cm	0.77	0.71	0.59	0.59	0.59	0.65
75	HWR 75cm pF6.2	SM75	0.75	0.73	0.56	0.57	0.57	0.65
10	WP 10cm	v 10 cm (m ns^{-1})	- 0.78	- 0.64	0.61	0.66	0.66	0.65
20	WP 20cm	SM20	0.78	0.69	0.61	0.61	0.61	0.65
20	HWR 20cm pF4.2	ε_r 20cm	0.76	0.72	0.58	0.58	0.58	0.65
10	WP 10cm	SM10	0.78	0.67	0.61	0.63	0.63	0.65
60	WP 60cm	v 60 cm (m ns^{-1})	- 0.79	- 0.67	0.62	0.62	0.62	0.65
60	HWR 60cm pF6.2	v 60 cm (m ns^{-1})	- 0.68	- 0.73	0.46	0.56	0.56	0.65
75	HWR 75cm pF4.2	ε_r 75cm	0.72	0.73	0.52	0.55	0.55	0.64
75	WP 75cm	SM75	0.75	0.72	0.56	0.56	0.56	0.64
30	WHC 30cm	alpha 30 cm (m^{-1})	0.77	0.69	0.59	0.59	0.59	0.64
10	WP 10cm	ε_r 10cm	0.77	0.69	0.59	0.59	0.59	0.64
60	WP 60cm	SM60	0.76	0.69	0.58	0.59	0.59	0.64
20	WP 20cm	v 20 cm (m ns^{-1})	- 0.78	- 0.66	0.61	0.62	0.62	0.64
30	HWR 30cm pF6.2	ε_r 30cm	0.75	0.70	0.57	0.57	0.57	0.64
60	WP 60cm	ε_r 60cm	0.73	0.70	0.53	0.56	0.56	0.63
30	HWR 30cm pF6.2	SM30	0.73	0.70	0.53	0.56	0.56	0.63
30	HWR 30cm pF4.2	sigma 30 cm (S m^{-1})	0.74	0.69	0.55	0.57	0.57	0.63